

QUENCHING AND ANISOTROPY OF HYDROMAGNETIC TURBULENT TRANSPORT

BIDYA BINAY KARAK¹, MATTHIAS RHEINHARDT², AXEL BRANDENBURG^{1,3}, PETRI J. KÄPYLÄ^{2,4}, AND MAARIT J. KÄPYLÄ⁴¹ Nordita, KTH Royal Institute of Technology and Stockholm University, Roslagstullsbacken 23, SE-10691 Stockholm, Sweden² Department of Physics, Gustaf Hållströmin katu 2a, P.O. Box 64, FI-00014 University of Helsinki, Finland³ Department of Astronomy, AlbaNova University Center, Stockholm University, SE-10691 Stockholm, Sweden⁴ ReSoLVE Centre of Excellence, Department of Information and Computer Science, Aalto University, P.O. Box 15400, FI-00076 Aalto, Finland

Received 2014 June 17; accepted 2014 August 20; published 2014 ???

ABSTRACT

Hydromagnetic turbulence affects the evolution of large-scale magnetic fields through mean-field effects like turbulent diffusion and the α effect. For stronger fields, these effects are usually suppressed or quenched, and additional anisotropies are introduced. Using different variants of the test-field method, we determine the quenching of the turbulent transport coefficients for the forced Roberts flow, isotropically forced non-helical turbulence, and rotating thermal convection. We see significant quenching only when the mean magnetic field is larger than the equipartition value of the turbulence. Expressing the magnetic field in terms of the equipartition value of the *quenched* flows, we obtain for the quenching exponents of the turbulent magnetic diffusivity about 1.3, 1.1, and 1.3 for Roberts flow, forced turbulence, and convection, respectively. However, when the magnetic field is expressed in terms of the equipartition value of the *unquenched* flows, these quenching exponents become about 4, 1.5, and 2.3, respectively. For the α effect, the exponent is about 1.3 for the Roberts flow and 2 for convection in the first case, but 4 and 3, respectively, in the second. In convection, the quenching of turbulent pumping follows the same power law as turbulent diffusion, while for the coefficient describing the $\mathbf{\Omega} \times \mathbf{J}$ effect nearly the same quenching exponent is obtained as for α . For forced turbulence, turbulent diffusion proportional to the second derivative along the mean magnetic field is quenched much less, especially for larger values of the magnetic Reynolds number. However, we find that in corresponding axisymmetric mean-field dynamos with dominant toroidal field the quenched diffusion coefficients are the same for the poloidal and toroidal field constituents.

Key words: convection – diffusion – dynamo – magnetic fields – magnetohydrodynamics (MHD) – turbulence

Online-only material: color figures

1. INTRODUCTION

Many astrophysical objects possess turbulent convection, and the dynamo mechanisms based on it are believed to be responsible for the generation and maintenance of the observed magnetic fields. The study of the dynamo mechanism in the solar convection zone using simulations of turbulent convection in spherical shells began in the 1980s with the works of Gilman & Miller (1981), Gilman (1983), and Glatzmaier (1985), and has recently been pursued further by many more authors (Brun et al. 2004; Racine et al. 2011; Käpylä et al. 2012, 2013; Karak et al. 2014). However, under stellar conditions the dimensionless parameters governing magnetohydrodynamics attain extreme values, which are far from being accessible through numerical models. So we do not know to what extent feasible models at temperate parameter regimes reflect properties of convection and dynamos in real stars. An alternative approach to studying the dynamo problem is mean-field theory, which began with the pioneering works of Parker (1955), Braginsky (1964), and Steenbeck et al. (1966). This approach is computationally less expensive because one does not need to resolve the full dynamical range of the small-scale turbulence, which is instead parameterized. In recent years, there have been significant achievements of mean-field MHD in reproducing various aspects of magnetic and flow fields in the Sun (e.g., Chatterjee et al. 2004; Rempel 2006; Käpylä et al. 2006; Choudhuri & Karak 2009, 2012; Karak 2010; Charbonneau 2010; Pipin & Kosovichev 2011).

In this context, an important task is to determine the mean electromotive force $\overline{\mathcal{E}}$, which results from the correlation be-

tween the fluctuating constituents of velocity and magnetic field, in terms of the mean field $\overline{\mathbf{B}}$. There is no accurate theory to accomplish this task from first principles, except for some limiting cases, in particular those of small Strouhal and magnetic Reynolds number, R_m . Therefore, suitable assumptions are required in determining $\overline{\mathcal{E}}$. When $\overline{\mathbf{B}}$ varies slowly in space and time, we may write

$$\overline{\mathcal{E}}_i = \alpha_{ij} \overline{B}_j + \beta_{ijk} \frac{\partial \overline{B}_j}{\partial x_k}. \quad (1)$$

The diagonal components of α_{ij} are usually the most important terms for dynamo action, but in the presence of shear, the $\mathbf{\Omega} \times \mathbf{J}$ (Krause & Rädler 1980) and shear-current (Rogachevskii & Kleeorin 2003) effects, both covered by β_{ijk} , can also enable it. Many components of β_{ijk} , however, describe dissipative effects.

Doubts can be raised regarding the explanatory and predictive power of mean-field dynamo models given that the tensors α_{ij} and β_{ijk} are often chosen to some extent arbitrarily or are even tuned to obtain results resembling features of the Sun. Therefore, methods to measure these coefficients from simulations have been developed. At present the most accurate method is the so-called test-field method (Schrinner et al. 2005, 2007; Brandenburg et al. 2008b, 2013). In this method, one selects an adequate number of independent mean fields, the “test fields,” and solves for each of them the corresponding equation for the fluctuating magnetic field (in addition to the main simulation). Finally, via computing the mean electromotive force, the transport coefficients are calculated.

There are different variants of the test-field method. The best established one is based on the average over two spatial (the

“horizontal”) coordinates. This method has been applied to a large variety of setups, e.g., isotropic homogeneous turbulence (Sur et al. 2008; Brandenburg et al. 2008b), homogeneous shear flow turbulence (Brandenburg et al. 2008a), with and without helicity (Mitra et al. 2009), turbulent convection (Käpylä et al. 2009a), and supernova-driven interstellar turbulence (Gressel et al. 2013). Another variant is based on Fourier-weighted horizontal averages and allows us to determine also the coefficients that multiply horizontal derivatives of the mean field. This method has been applied to forced turbulence (Brandenburg et al. 2012) and to cosmic-ray-driven turbulence (Rogachevskii et al. 2012; Bykov et al. 2013).

In dynamo models based on thin flux tubes, forming the major alternative to distributed turbulent dynamos, the magnetic field strength in the deep parts of the solar convection zone is believed to exceed its value at equipartition with velocity (Choudhuri & Gilman 1987; D’Silva & Choudhuri 1993; Weber et al. 2011). On the other hand, it is well known that turbulent transport becomes less efficient when the mean magnetic field’s strength is comparable to or larger than the equipartition value. Therefore, precise knowledge of this “quenching” is needed. Mean-field dynamo models of the $\alpha\Omega$ type often employ an “ad hoc” algebraic or dynamical α -quenching (Jepps 1975; Covas et al. 1998), while largely ignoring the quenching of the turbulent diffusivity η_t despite its importance in determining the cycle frequency. Indeed, in the absence of quenching, the standard estimate of η_t for the Sun ($\sim 10^{12}$ – 10^{13} cm² s^{−1}) yields a rather short cycle period of 2–3 yr (Köhler 1973). However, by considering the quenching of η_t , a reasonable value of the cycle period can easily be obtained (Rüdiger et al. 1994; Guerrero et al. 2009; Muñoz-Jaramillo et al. 2011). In fact, measuring the cycle frequency in a simulation has been one way of determining the quenching of η_t (Käpylä & Brandenburg 2009).

Early work by Moffatt (1972) and Rüdiger (1974) showed that under the Second Order Correlation Approximation (SOCA), α is quenched inversely proportional to the third power of the magnetic field. Following Vainshtein & Cattaneo (1992), several investigations have suggested that α is beginning to be quenched noticeably when the mean field becomes comparable to R_m^{-1} times the equipartition value (Cattaneo & Hughes 1996), i.e., for extremely weak magnetic fields. This behavior is also called “catastrophic quenching.” However, it is now understood as an artifact of having defined volume-averaged mean fields (Brandenburg 2001; Brandenburg et al. 2008b) combined with the usage of perfectly conducting or periodic boundary conditions and is not expected to be important in astrophysical bodies where magnetic helicity fluxes can alleviate catastrophic quenching (e.g., Kleeorin et al. 2000; Del Sordo et al. 2013). The actual value of α shows a much weaker dependence on R_m even when \bar{B} is comparable with the equipartition value (Brandenburg et al. 2008b). This work also shows that the R_m dependence of α and η_t is such that in a saturated state their contributions to the growth rate nearly balance, with a residual matching the microscopic resistive term. Consequently, the saturated mean electromotive force is proportional to R_m^{-1} , which is sometimes misinterpreted as catastrophic quenching.

Once catastrophic quenching is alleviated, the magnetic field can grow to equipartition field strengths, when other quenching mechanisms that are not R_m dependent might become important and can therefore be studied already for smaller values of R_m . Sur et al. (2007) found that α is quenched proportional to $1/\bar{B}^2$

and $1/\bar{B}^3$ for time-dependent and steady flows, respectively. Their latter result was based on analytic theory and appeared to be confirmed by numerical simulations using a steady forcing proportional to the ABC-flow. However, subsequent work by Rheinhardt & Brandenburg (2010) demonstrated quenching proportional to \bar{B}^{-4} for a steady forcing proportional to the flow I of Roberts (1972), hereafter referred to as Roberts flow. They also noted that for ABC-flow forcing the quenching is indeed better described when setting the power also to 4 instead of 3. More recently, in supernova-driven turbulent dynamo simulations, Gressel et al. (2013) find $\alpha \sim (\bar{B}/B_{\text{eq}})^{-2}$, where B_{eq} is the local equipartition value.

For the turbulent diffusivity, Kitchatinov et al. (1994) and Rogachevskii & Kleeorin (2000) obtained that η_t is quenched inversely proportional to \bar{B} . In the two-dimensional case, Cattaneo & Vainshtein (1991) have found catastrophic quenching of η_t . However, this is a special situation connected with the fact that in two dimensions the mean square vector potential is a conserved quantity. This is no longer the case in three dimensions. Quenching similar to Kitchatinov et al. (1994) has been confirmed by simulations (Brandenburg 2001; Blackman & Brandenburg 2002; Gressel et al. 2013). In particular, making the ansatz $\eta_t \sim 1/(1 + p(\bar{B}/B_{\text{eq}})^q)$, Gressel et al. (2013) find $q \approx 1$ in supernova-driven simulations of the turbulent interstellar medium. On the other hand, Yousef et al. (2003) find $q \approx 2$ in simulations of forced turbulence with a decaying large-scale magnetic field. However, Käpylä & Brandenburg (2009) found that their results depend on the strength of shear with $q \approx 1$ for weak shear while $q \approx 2$ for strong shear.

In the present work we measure the quenching of these transport coefficients as a function of the mean magnetic field strength for three different background simulations: (1) forced Roberts flow, (2) forced turbulence in a triply periodic box, and (3) convection in a bounded box. In all these simulations, we impose a uniform and constant external mean field. However, this induces a preferred direction that causes the *statistical properties* of the turbulence to be axisymmetric with respect to the direction of the magnetic field. In the following, we refer to such flows as *axisymmetric turbulence*, for which the number of independent components of the α and η tensors is reduced to only nine, simplifying also their determination (Brandenburg et al. 2012).

2. CONCEPT OF TURBULENT TRANSPORT IN MEAN-FIELD DYNAMO

The evolution of the magnetic field \mathbf{B} in an electrically conducting fluid is governed by the induction equation

$$\frac{\partial \mathbf{B}}{\partial t} = \nabla \times (\mathbf{U} \times \mathbf{B} - \eta \mathbf{J}), \quad (2)$$

where \mathbf{U} is the fluid velocity. Here, η is the microphysical magnetic diffusivity, while the magnetic permeability of the fluid has been set to unity. Thus, the current density \mathbf{J} is given by $\mathbf{J} = \nabla \times \mathbf{B}$. In mean-field MHD, we consider the fields as sums of “averaged” and small-scale “fluctuating” fields, with the assumption that the averaging satisfies (at least approximately) the Reynolds rules. Denoting averaged fields by overbars and fluctuating ones by lowercase letters, we write the equation for the mean magnetic field $\bar{\mathbf{B}}$ as

$$\frac{\partial \bar{\mathbf{B}}}{\partial t} = \nabla \times (\bar{\mathbf{U}} \times \bar{\mathbf{B}} + \bar{\boldsymbol{\varepsilon}} - \eta \bar{\mathbf{J}}), \quad (3)$$

where $\bar{\mathcal{E}} = \overline{\mathbf{u} \times \mathbf{b}}$ is the aforementioned mean electromotive force, which captures the correlation of the fluctuating fields \mathbf{u} and \mathbf{b} . The ultimate goal of mean-field MHD is to express $\bar{\mathcal{E}}$ in terms of $\bar{\mathbf{B}}$ itself. There are several procedures for doing that. When the mean magnetic field varies slowly in space and time we can write $\bar{\mathcal{E}}$ in the form of Equation (1). Our primary goal is to measure the transport coefficients α_{ij} and β_{ijk} in the presence of an imposed uniform magnetic field \mathbf{B}_{ext} and, in particular, to measure the degree of their quenching and anisotropy.

Let us consider turbulence that is anisotropic and exhibiting only one preferred direction $\hat{\mathbf{e}}$, referring to an external magnetic field, rotation axis, or the direction of gravity. Then following Brandenburg et al. (2012), the general representation of $\bar{\mathcal{E}}$ is given by

$$\begin{aligned} \bar{\mathcal{E}} = & \alpha_{\perp} \bar{\mathbf{B}} + (\alpha_{\parallel} - \alpha_{\perp})(\hat{\mathbf{e}} \cdot \bar{\mathbf{B}})\hat{\mathbf{e}} + \gamma \hat{\mathbf{e}} \times \bar{\mathbf{B}} \\ & - \eta_{\perp} \bar{\mathbf{J}} - (\eta_{\parallel} - \eta_{\perp})(\hat{\mathbf{e}} \cdot \bar{\mathbf{J}})\hat{\mathbf{e}} - \delta \hat{\mathbf{e}} \times \bar{\mathbf{J}} \\ & - \kappa_{\perp} \bar{\mathbf{K}} - (\kappa_{\parallel} - \kappa_{\perp})(\hat{\mathbf{e}} \cdot \bar{\mathbf{K}})\hat{\mathbf{e}} - \mu \hat{\mathbf{e}} \times \bar{\mathbf{K}} \end{aligned} \quad (4)$$

with nine coefficients α_{\perp} , α_{\parallel} , \dots , μ . While $\bar{\mathbf{J}}$ is given by the antisymmetric part of the gradient tensor $\nabla \bar{\mathbf{B}}$, $\bar{\mathbf{K}}$ is defined by $\bar{\mathbf{K}} = \hat{\mathbf{e}} \cdot (\nabla \bar{\mathbf{B}})^S$, with $(\nabla \bar{\mathbf{B}})^S$ being the symmetric part of $\nabla \bar{\mathbf{B}}$. For homogeneous isotropic turbulence, $\alpha_{\parallel} = \alpha_{\perp}$, $\eta_{\parallel} = \eta_{\perp}$, and the other coefficients vanish. We note that our sign convention for α_{\perp} , α_{\parallel} , and γ follows that commonly used, but it differs from that used in Brandenburg et al. (2012).

The μ term corresponds to a modification of turbulent diffusion along the preferred direction. To understand this, let us assume that only η_{\perp} , η_{\parallel} , and μ are non-vanishing and independent of position. By introducing the quantities $\eta_T \equiv \eta_t + \eta$, with $\eta_t \equiv \eta_{\perp} - \mu/2$, and $\epsilon \equiv \eta_{\parallel} - \eta_{\perp} + \mu/2$, we have

$$\frac{\partial \bar{\mathbf{B}}}{\partial t} = \eta_T \nabla^2 \bar{\mathbf{B}} + \mu \nabla_{\parallel}^2 \bar{\mathbf{B}} + \epsilon (\nabla_{\perp}^2 \bar{\mathbf{B}}_{\perp} + \nabla_{\perp} \nabla_{\parallel} B_{\parallel}), \quad (5)$$

which shows that positive values of μ correspond to an enhancement of turbulent diffusion along the preferred direction. As Equation (5) reveals, η_{\parallel} and η_{\perp} do not characterize the diffusion parallel and perpendicular to the preferred direction, as their symbols might suggest.

An anisotropy similar to that of Equation (5) has been considered in connection with the turbulent decay of sunspot magnetic fields (Rüdiger & Kitchatinov 2000), where the mean magnetic field defines the preferred direction. It has not yet been used in mean-field dynamo models, where, however, anisotropies of the turbulent diffusivity due to the simultaneous influence of rotation and stratification have been taken into account (Rüdiger & Brandenburg 1995; Pipin & Kosovichev 2014).

3. THE MODEL SETUP

We distinguish two basically different schemes of establishing the background flow: by a prescribed forcing or by the convective instability. In the first case, both laminar and turbulent (artificially forced) flows will be considered. With respect to the fluid, we generally think of an ideal gas with state variables density ρ , pressure p , and temperature T , adopting, however, different effective equations of state for the two schemes.

The continuity and induction equations are shared by both schemes and take the form

$$\frac{D \ln \rho}{Dt} = -\nabla \cdot \mathbf{U}, \quad (6)$$

$$\frac{\partial \mathbf{A}}{\partial t} = \mathbf{U} \times \mathbf{B} + \eta \nabla^2 \mathbf{A}. \quad (7)$$

Here $D/Dt = \partial/\partial t + \mathbf{U} \cdot \nabla$ is the advective time derivative and \mathbf{A} is the magnetic vector potential. The magnetic field includes the imposed field, i.e., $\mathbf{B} = \mathbf{B}_{\text{ext}} + \nabla \times \mathbf{A}$, and the microscopic diffusivity η is constant.

3.1. Forced Flows

In these models, we assume the fluid to be isothermal, which implies for its equation of state $p = c_s^2 \rho$, with the constant sound speed c_s . Hence, we solve Equations (6) and (7) together with the momentum equation,

$$\frac{D\mathbf{U}}{Dt} = -c_s^2 \nabla \ln \rho + \rho^{-1} (\mathbf{J} \times \mathbf{B} + \nabla \cdot 2\nu \mathbf{S}) + \mathbf{f}. \quad (8)$$

Here $\nu = \text{const}$ is the kinematic viscosity, and \mathbf{f} is a forcing function to be specified below. The traceless rate of strain tensor \mathbf{S} is given by

$$S_{ij} = \frac{1}{2}(U_{i,j} + U_{j,i}) - \frac{1}{3}\delta_{ij} \nabla \cdot \mathbf{U}, \quad (9)$$

where the commas denote partial differentiation with respect to the coordinate j or i .

The simulation domain for this model is periodic in all directions with dimension $L_x \times L_y \times L_z$. In the following we always use $L_x = L_y \equiv L$ and express lengths in units of the inverse of the wavenumber $k_1 = 2\pi/L$.

3.1.1. Roberts Forcing

First, we use a laminar forcing to maintain one of the flows for which Roberts (1972) had demonstrated dynamo action, namely, his flow I. It is incompressible, independent of z , and all second-rank tensors obtained from it by xy averaging are symmetric about the z -axis (Rädler et al. 2002). The flow is defined by

$$\mathbf{u}_0 = -\hat{\mathbf{z}} \times \nabla \psi + k_f \psi \hat{\mathbf{z}}, \quad (10)$$

where

$$\psi = (u_0/k_0) \cos k_0 x \cos k_0 y, \quad k_f = \sqrt{2} k_0, \quad (11)$$

with constant u_0 and k_0 . Note that this flow is maximally helical, i.e., $\nabla \times \mathbf{u}_0 = k_f \mathbf{u}_0$. We define the forcing \mathbf{f} such that for $\mathbf{B} = \mathbf{0}$, the flow (10) with $\rho = \rho_0 = \text{const}$ is an exact solution of Equation (8):

$$\mathbf{f} = \nu k_0^2 \mathbf{u}_0 + \mathbf{u}_0 \cdot \nabla \mathbf{u}_0 \quad (= \nu k_0^2 \mathbf{u}_0 + \frac{1}{2} \nabla u_0^2). \quad (12)$$

We perform several simulations with different strengths of the external magnetic field \mathbf{B}_{ext} with this forcing.

3.1.2. Forced Turbulence

Here we employ for \mathbf{f} a random forcing function, namely, a linearly polarized wave with wavevector and phase being changed randomly between integration timesteps (Brandenburg 2001). The driven flow is non-helical and known to lack an α effect (Brandenburg et al. 2008a). The averaged modulus of the wavevector is denoted by k_f , and the ratio k_f/k_1 is referred to as the scale separation ratio. To achieve sufficiently large scale separation, we would need to keep k_f/k_1 large. However, in this case $R_m = u_{\text{rms}}/\eta k_f$ becomes small. Therefore, we use $k_f/k_1 \geq 5$ as a compromise.

3.2. Convection

In this model the background flow is generated by convection and consequently we employ $p = (c_p - c_v)\rho T$ for the equation of state of the fluid, where c_p and c_v are the specific heats at constant pressure and volume, respectively. Our model is similar to many earlier studies in the literature (e.g., Brandenburg et al. 1996; Ossendrijver et al. 2001; Käpylä et al. 2008; Käpylä et al. 2009a, 2009b). Its computational domain is a rectangular box consisting of three layers: the lower part ($-0.85 \leq z/d < 0$) is a convectively stable overshoot layer, the middle part ($0 \leq z/d \leq 1$) is convectively unstable, and the upper part ($1 < z/d \leq 1.15$) is an almost isothermal cooling layer. The overshoot layer was made comparatively thick to guarantee that the overshooting is not affected by the lower boundary. The box dimensions are $(L_x, L_y, L_z) = (5, 5, 2)d$, where d is the depth of the unstable layer. Gravity is acting in the downward direction (i.e., along the negative z direction). By including rotation about the z -axis, we can consider the simulation box as a small portion of a star located at one of its poles. The mass conservation and induction equations (6) and (7) are now complemented by a modified momentum equation and an equation for the internal energy per unit mass (Brandenburg et al. 1996)

$$\begin{aligned} \frac{DU}{Dt} &= -\frac{\nabla p}{\rho} + \mathbf{g} - 2\boldsymbol{\Omega} \times \mathbf{U} + \frac{1}{\rho}(\mathbf{J} \times \mathbf{B} + \nabla \cdot 2\nu\rho\mathbf{S}), \quad (13) \\ \frac{De}{Dt} &= -\frac{p}{\rho}\nabla \cdot \mathbf{U} + \frac{1}{\rho c_v}\nabla \cdot K(z)\nabla e + 2\nu\mathbf{S}^2 + \frac{\eta\mu_0}{\rho}\mathbf{J}^2 - \frac{e-e_0}{\tau(z)}. \end{aligned}$$

Here, $\mathbf{g} = -g\hat{\mathbf{z}}$, with $g > 0$, is the gravitational acceleration; $\boldsymbol{\Omega} = \Omega_0(-\sin\theta, 0, \cos\theta)$ is the rotation vector, with θ its angle against the z direction; and K is the heat conductivity with a piecewise constant z profile to be specified below. The specific internal energy is related to the temperature via $e = c_v T$. In the energy equation (13), the last term is of relaxation type and regulates the internal energy to settle on average close to $e_0 = \text{const}$. As there is permanent heat input from the lower boundary and from viscous heating, it effectively acts as a cooling. The relaxation rate $\tau(z)^{-1}$ has a value of $75\sqrt{g/d}$ within the cooling layer and drops smoothly to zero within the unstable layer over a transition zone of width $0.025d$.

The vertical boundary conditions for the velocity are chosen to be impenetrable and stress free, i.e.,

$$U_{x,z} = U_{y,z} = U_z = 0, \quad (14)$$

while for the magnetic field we use the vertical field boundary condition $B_x = B_y = 0$. A steady influx of heat $F_0 = -(K\partial_z e)(x, y, -0.85d)/c_v$ at the bottom of the box and a constant temperature, i.e., constant internal energy, at its top are maintained, where the latter is specified to be just equal to e_0 occurring in the relaxation term. The x and y directions are periodic for all fields.

The input parameters are now determined in the following somewhat indirect way: Instead of prescribing K , it is assumed that the hydrostatic reference solution coincides in the overshoot and unstable layers with a polytrope, the index m of which is prescribed. Here we choose $m = 3$ and $m = 1$, respectively. As for a polytrope $de/dz = -g/(m+1)(\gamma-1)$, $\gamma = c_p/c_v$, and at each z we have $F_0 = -(K/c_v)de/dz = \text{const}$, the heat conductivity is obtained as $K = c_v(m+1)(\gamma-1)F_0/g$, i.e., it is also piecewise constant (for a physical motivation, see Hurlburt et al. 1986). For simplicity it is assumed that in the cooling layer, for which no polytrope exists, K has the same value

as in the unstable one. Within the ranges of the other control parameters covered by our simulations, it is then guaranteed that the relaxation to the quasi-isothermal state is dominated by the term $-e/\tau$.

The convection problem is governed by a set of dimensionless control parameters comprising the Prandtl, Taylor, and Rayleigh numbers

$$\text{Pr} = \frac{\nu}{\chi(z_m)}, \quad \text{Ta} = \frac{4\Omega^2 d^4}{\nu^2}, \quad (15)$$

$$\text{Ra} = \frac{gd^4}{\nu\chi(z_m)H_p(z_m)}\Delta\nabla(z_m), \quad (16)$$

along with the dimensionless pressure scale height at the top

$$\xi_0 = (\gamma - 1)e_0/gd. \quad (17)$$

For the calculation of the Prandtl and Rayleigh numbers, the values of the thermal diffusivity $\chi = K/\rho c_p$, the superadiabatic gradient $\Delta\nabla = d(s/c_p)/d \ln p$ and the pressure scale height H_p of the associated hydrostatic equilibrium solution are taken from the middle of the convective layer at $z_m = d/2$. The density contrast within the unstable layer is

$$\frac{\rho(0)}{\rho(d)} = 1 + \frac{gd}{2(\gamma - 1)e_0} = 1 + \frac{1}{2\xi_0}. \quad (18)$$

Hence, the parameter ξ_0 controls the density stratification in our domain. We use $\xi_0 = 3/25$ in all the simulations, which results in a (hydrostatic) density contrast of $31/6$; γ was fixed to $5/3$ throughout, and the different models have the same initial density at $z = z_m$.

Equation (18) assumes that $e = e_0$ at the top of the convective layer, which cannot be exactly true. In the simulations this error is increased by the fact that the effect of the cooling reaches somewhat below $z/d = 1$. This leads to a higher density contrast (≈ 8) in the actual hydrostatic solution.

3.3. Diagnostics

As diagnostics we use the fluid and magnetic Reynolds numbers

$$\text{Re} = \frac{u_{\text{rms}}}{\nu k_f}, \quad R_m = \frac{u_{\text{rms}}}{\eta k_f}, \quad (19)$$

where for the convection setup $k_f = 2\pi/d$ is an estimate of the wavenumber of the largest energy-carrying eddies. $u_{\text{rms}} = \langle u^2 \rangle^{1/2}$ is the rms value of the velocity, with $\langle \cdot \rangle$ denoting the average over the whole box or, for the convection setup, over the unstable layer only, i.e., $0 \leq z/d \leq 1$. The U_{rms} values for $B_{\text{ext}} = 0$, i.e., for the unquenched state, are marked by the subscript 0. For R_m we quote both the unquenched value, denoted by R_{m0} , and the quenched value for the run with the strongest field strength.

All simulations are performed using the PENCIL CODE,⁵ which uses sixth-order finite differences in space and a third-order-accurate explicit time stepping method.

⁵ <http://pencil-code.googlecode.com>

3.4. Test-field Methods

The goal of the test-field method is to measure the turbulent transport coefficients completely from given flow fields \mathbf{U} , which can either be prescribed explicitly or produced by a numerical simulation, called the *main run*. To accomplish this, the equation for the fluctuating fields

$$\frac{\partial \mathbf{a}^T}{\partial t} = \bar{\mathbf{U}} \times \mathbf{b}^T + \mathbf{u} \times \bar{\mathbf{B}}^T + (\mathbf{u} \times \mathbf{b}^T)' + \eta \nabla^2 \mathbf{a}^T \quad (20)$$

is solved for a set of prescribed *test fields* $\bar{\mathbf{B}}^T$. Here $\mathbf{b}^T = \nabla \times \mathbf{a}^T$ and the prime denotes the operation of extracting the fluctuation of a quantity. Each \mathbf{a}^T results in a mean electromotive force

$$\bar{\mathcal{E}}^T = \overline{\mathbf{u} \times \mathbf{b}^T}, \quad (21)$$

and if the test fields are independent and their number is adjusted to that of the desired components in α_{ij} and β_{ijk} , they can be obtained unambiguously from the system (21). For the truncated ansatz (1), test fields that depend linearly on position are suitable. However, when truncation is to be overcome, Equation (1) can be considered as the Fourier space representation of the most general $\bar{\mathcal{E}}-\bar{\mathbf{B}}$ relationship. Then α_{ij} and β_{ijk} are functions of wavevector \mathbf{k} and angular frequency ω of the Fourier transform and it is natural to specify the test fields to be harmonic in space (Brandenburg et al. 2008c) and time (Hubbard & Brandenburg 2009). By varying their \mathbf{k} and ω , arbitrarily close approximations to the general $\bar{\mathcal{E}}-\bar{\mathbf{B}}$ relationship can be obtained (see, e.g., Rheinhardt & Brandenburg 2012; Rädler 2014).

3.4.1. Test-field Method for Horizontal (z -dependent) Averages

We will employ two different flavors of the test-field method. For the first one we define mean quantities by averaging over all x and y . Then, necessarily, $\bar{B}_z = \text{const}$ and for homogeneous turbulence it is sufficient to consider horizontal mean fields $\bar{\mathbf{B}} = (\bar{B}_x(z, t), \bar{B}_y(z, t), 0)$ only. When restricting ourselves to the limit of stationarity, our \mathbf{k} -dependent test fields have the following form:

$$\begin{aligned} \bar{\mathbf{B}}^{1c} &= B_0(\cos kz, 0, 0), & \bar{\mathbf{B}}^{2c} &= B_0(0, \cos kz, 0), \\ \bar{\mathbf{B}}^{1s} &= B_0(\sin kz, 0, 0), & \bar{\mathbf{B}}^{2s} &= B_0(0, \sin kz, 0), \end{aligned} \quad (22)$$

where $k = k_z$ and in most of the simulations we use $k = k_1$. The z component of $\bar{\mathcal{E}}$ does not influence $\bar{\mathbf{B}}$; thus, only its x and y components matter and we have

$$\bar{\mathcal{E}}_i = \alpha_{ij} \bar{B}_j - \eta_{ij} \bar{J}_j, \quad (23)$$

with $i, j = 1, 2$ and $\eta_{i1} = \beta_{i23}$ and $\eta_{i2} = -\beta_{i13}$. That is, we can derive eight coefficients (four α and four η) using the above test fields. Our main interest is to compute the diagonal components of α_{ij} and η_{ij} . However, in some cases we also study the off-diagonal components. Since the resulting turbulent transport coefficients depend only on z (in addition to t), we call this variant of the test-field method TFZ. It is implemented in the PENCIL CODE and discussed in detail by Brandenburg et al. (2008a).

It is convenient to discuss the results in terms of the quantities

$$\begin{aligned} \alpha &= \frac{1}{2}(\alpha_{11} + \alpha_{22}), & \gamma &= \frac{1}{2}(\alpha_{21} - \alpha_{12}), \\ \eta_t &= \frac{1}{2}(\eta_{11} + \eta_{22}), & \delta &= \frac{1}{2}(\eta_{21} - \eta_{12}), \end{aligned} \quad (24)$$

which cover an important subset of the eight coefficients.

3.4.2. Test-field Method for Axisymmetric Turbulence

Next, we turn to another variant of the test-field method that allows us to calculate all nine coefficients in Equation (4) under the restriction of axisymmetric turbulence. It is then necessary to consider mean fields that depend on more than one dimension, as otherwise the gradient tensor $\nabla \bar{\mathbf{B}}$ can be expressed completely by the components of \mathbf{J} and the coefficients κ_\perp , κ_\parallel , and μ cannot be separated from η_\perp , η_\parallel , and δ . Hence, we now admit mean fields depending on all three spatial coordinates and define the mean by *spectral filtering*. We specify it such that only field constituents whose components $\sim \sum_j c_j(z) \exp i\bar{\mathbf{k}}_j \cdot \mathbf{x}_\perp$ contribute to the mean. Here $\mathbf{x}_\perp = (x, y)$ is the position vector in horizontal planes and the sum is over all two-dimensional wavevectors $\bar{\mathbf{k}}_j$ of the form $(\pm \bar{k}_x, \pm \bar{k}_y)$ with fixed $\bar{k}_x, \bar{k}_y > 0$. So averaging means here to perform the operation

$$\bar{f}(x, y, z) = \frac{1}{A} \sum_j \int_A f(x', y', z) e^{i\bar{\mathbf{k}}_j \cdot (\mathbf{x}_\perp - \mathbf{x}'_\perp)} dx' dy', \quad (25)$$

where A is the horizontal cross-section of the box. We call this variant of the test-field method for axisymmetric turbulence TFA and refer for further details to Brandenburg et al. (2012). In our case, the preferred direction is given by that of the externally imposed magnetic field.

As we will apply this method only with horizontally isotropic periodic boxes with $L_x = L_y = L$, we may choose $\bar{k}_x = \bar{k}_y = k_1 = 2\pi/L$. In general, it does not make much sense to choose \bar{k}_x or \bar{k}_y different from these smallest possible values for the corresponding extents of a given box. Otherwise, possible field constituents with smaller wavenumbers would be counted to the “fluctuations,” which is hardly desirable. Even for our choice $\bar{k}_x, \bar{k}_y = k_1$ this could be a problem, namely, with respect to constituents with horizontal wavenumber k_x or k_y equal to zero, so their occurrence should be avoided. As we apply TFA only to homogeneous turbulence (fully periodic boxes), this is granted.

Spectral filtering, being clearly useful for comparisons with observations, is known to violate in general the Reynolds rule $\overline{Fg} = 0$. However, if in the \mathbf{k} spectrum of the quantity $G = \bar{G} + g$ there are “gaps” at $k_x, k_y = 2k_1$ (for our choice) with vanishing spectral amplitudes, this rule is granted.⁶ Such gaps, albeit only in the form of amplitude depressions, can emerge in the saturated stage of a turbulent dynamo; see Brandenburg (2001) for examples, where this phenomenon was characterized as “self-cleaning.” In the kinematic stage, on the other hand, gaps cannot be expected and it remains unclear to what extent a mean-field approach, based on spectral filtering, can then be useful.

In this method, we use four test fields defined by

$$\begin{aligned} \bar{\mathbf{B}}^{1c} &= (B_0 \cos k_x x, 0, 0), & \bar{\mathbf{B}}^{1s} &= (B_0 \sin k_x x, 0, 0), \\ \bar{\mathbf{B}}^{2c} &= (0, 0, B_0 \cos k_y y), & \bar{\mathbf{B}}^{2s} &= (0, 0, B_0 \sin k_y y), \end{aligned} \quad (26)$$

where B_0 is a constant and we have used the abbreviations

$$\begin{aligned} \cos &= \cos \bar{k}_x x, & \sin &= \sin \bar{k}_x x, \\ \cos &= \cos k_z z, & \sin &= \sin k_z z. \end{aligned} \quad (27)$$

Note the different roles of the wavenumbers: while \bar{k}_x and \bar{k}_y are *defining* the mean, by k_z a specific mean field out of the

⁶ To let Equation (20) hold, we need also $\bar{\mathbf{U}} = \mathbf{0}$, otherwise a term $(\bar{\mathbf{U}} \times \bar{\mathbf{B}})'$ would show up.

Table 1
Summary of the Runs

Set	Description	$\hat{\mathbf{B}}_{\text{ext}}$	TFM	R_{m0}	R_m^{min}	P_m	$B_{\text{eq}0}$	p_α	p_γ	p_η	p_δ	q_α	q_γ	q_η	q_δ
RF1	Forced Roberts flow	$\hat{\mathbf{x}}$	TFZ	0.88	0.0002	1.0	0.010	0.59	...	0.59	...	1.3	...	1.3	...
RF2	Forced Roberts flow	$\hat{\mathbf{x}}$	TFZ	0.707	0.10	1.0	1.000	0.3	...	0.4	...	1.3	...	1.3	...
TBx	Forced turbulence ($k_f = 5k_1$)	$\hat{\mathbf{x}}$	TFZ	0.87	0.71	1.0	0.045	0.38	1.1	...
TBz	Forced turbulence ($k_f = 5k_1$)	$\hat{\mathbf{z}}$	TFZ	0.87	0.71	1.0	0.045	0.21	1.1	...
AT1	Forced turbulence ($k_f = 27k_1$)	$\hat{\mathbf{z}}$	TFA	2.23	1.67	1.0	0.060	0.66	1.2	...
AT2	Forced turbulence ($k_f = 27k_1$)	$\hat{\mathbf{z}}$	TFA	18.2	15.8	1.0	0.100	2.50	1.0	...
AT3	Forced turbulence ($k_f = 27k_1$), $B_{\text{ext}}/B_{\text{eq}} \approx 4.3$ fixed	$\hat{\mathbf{z}}$	TFA		0.08 – 537 ^a	1.0	0.022 – 0.116 ^b
CR0	Non-rotating convection	$\hat{\mathbf{z}}$	TFZ	3.91	0.5	0.8	0.087	...	0.34	0.34	1.2	1.2	...
CR1	Rotating convection	$\hat{\mathbf{x}}$	TFZ	3.85	0.7	0.8	0.087	0.11	0.12	0.20	0.02	1.8	1.4	1.3	2.0
CR2	Rotating convection	$\hat{\mathbf{x}}$	TFZ	11.7	0.2	5.0	0.054	0.14	0.11	0.10	0.06	1.8	1.3	1.3	1.8
CR3	Rotating convection	$\hat{\mathbf{x}}$	TFZ	20.2	6.0	3.0	0.090	0.25	0.24	0.65	0.06	2.0	1.3	1.3	2.0
CR4	Rotating convection	$\hat{\mathbf{x}}$	TFZ	29.1	3.3	5.0	0.065	0.17	0.15	0.16	0.07	2.0	1.3	1.3	1.8
CR5	Rotating convection	$\hat{\mathbf{x}}$	TFZ	89.5	19.2	5.0	0.082	0.24	0.23	0.37	0.12	1.8	1.24	1.26	1.7
CR1Bz	As CR1	$\hat{\mathbf{z}}$	TFZ	3.85	0.13	0.8	0.088	0.65	0.12	0.41	1.0	1.3	1.3	1.3	1.8
CR3Bz	As CR3	$\hat{\mathbf{z}}$	TFZ	28.6	0.08	5.0	0.065	0.59	0.21	0.41	0.25	1.3	1.4	1.3	2.0
CR6	As CR1, uniform test fields	$\hat{\mathbf{x}}$	TFZ	3.85	0.70	0.8	0.087	0.16	0.11	2.0	1.4
CR7	As CR2, uniform test fields	$\hat{\mathbf{x}}$	TFZ	29.1	3.2	5.0	0.065	0.16	0.16	2.0	1.3

Notes. Data given for the stationary (Sets RF1 and RF2) or statistically saturated state, respectively. q_α , q_γ , q_η , and q_δ are the quenching exponents for α , γ , η , and δ , respectively, according to Equation (32). For RF1: $u_0 = 0.01c_s$, $\eta = 0.008c_s/k_1$, RF2: $u_0 = 1.0c_s$, $\eta = c_s/k_1$, CR0: Ra, Pr = 3×10^5 , 3.95, CR1: Ta, Ra, Pr = 5.6×10^3 , 3×10^5 , 3.95, CR2: Ta, Ra, Pr = 6.4×10^5 , 3×10^5 , 4.94, CR3: Ta, Ra, Pr = 1.0×10^4 , 4×10^5 , 2.93, CR4: Ta, Ra, Pr = 2.6×10^6 , 5×10^5 , 2.44, CR5: Ta, Ra, Pr = 1.6×10^7 , 1×10^6 , 0.97. Resolutions used are RF1: 96^3 , RF2: 144^3 , TBx, TBz: 256^3 , AT1: 128^3 , AT2: 360^3 , AT3: 72^3 to 672^3 CR0-CR7: 128^3 . R_m^{min} – minimal, i.e., maximally quenched R_m within a Set.

^a Not the minimum, but the range of values of the individual runs.

^b B_{eq} instead of $B_{\text{eq}0}$.

infinitude of possible ones is selected.⁷ Other than what could be expected, three test fields are in general not sufficient to calculate the wanted nine coefficients, as the linear system from which they are obtained suffers from a rank defect. For *homogeneous* turbulence, however, exploiting the orthogonality of the harmonic functions, even only two test fields were sufficient.

3.4.3. Computing Transport Coefficients via Resetting

At large R_m , we often find the solutions \mathbf{a}^T of the test problems (20) to grow rapidly due to the occurrence of unstable eigenmodes of the test problems' homogeneous parts. Therefore, similar to earlier studies (Sur et al. 2008; Mitra et al. 2009; Käpylä et al. 2009a; Hubbard et al. 2009), we reset \mathbf{a}^T to zero after a certain time interval to prevent the unstable eigenmodes from dominating and thus contaminating the coefficients. If the growth rates are not too high, after an initial transient phase, “plateaus” can be identified in the time series of the coefficients, during which they are essentially determined by the *bounded* solutions of the (inhomogeneous) problems (20). Even for monotonically growing \mathbf{a}^T , sufficiently long plateaus occur as the averaging in the determination of $\bar{\mathcal{E}}^T$ (Equation (21)) is capable of eliminating the unstable eigenmodes. Typically we use data from 10 such plateaus to compute the temporal averages of the transport coefficients and ensure by spot checks that the results do not depend on the length of the resetting interval.

⁷ Horizontal averaging with TFZ is equivalent to spectral filtering with TFA using $\bar{k}_x = \bar{k}_y = 0$. In that special case, all Reynolds rules are obeyed. In Brandenburg et al. (2012), c_x and c_y were replaced by $\sin \bar{k}_x x$ and $\sin \bar{k}_y y$, respectively. This is equivalent to the former, except that then TFZ cannot be recovered for $k_x = k_y = 0$.

4. RESULTS

4.1. Roberts Flow

We describe here results for Roberts flow forcing for two different parameter combinations (Sets RF1 and RF2 in Table 1). For RF1 we choose $u_0 = 0.01c_s$ and $\eta = \nu = 0.008c_s/k_1$, whereas for RF2 $u_0 = c_s$ and $\eta = \nu = c_s/k_1$, using $k_0 = k_1$ for both. With a vertical field, $\mathbf{B}_{\text{ext}} = B_{\text{ext}}\hat{\mathbf{z}}$, we have $\nabla \times (\mathbf{u}_0 \times \mathbf{B}_{\text{ext}}) = \mathbf{B}_{\text{ext}} \cdot \nabla \mathbf{u}_0 = \mathbf{0}$. Hence, there is no tangling of the field and consequently no effect of \mathbf{B}_{ext} on the flow, that is, no quenching. (Should, however, the flow have undergone a bifurcation and thus deviate from Equation (10), this need no longer be true. Yet, for the fluid Reynolds numbers considered in this paper we have not noticed any bifurcations.) Therefore, we choose a horizontal field $\mathbf{B}_{\text{ext}} = B_{\text{ext}}\hat{\mathbf{x}}$. We apply the TFZ procedure with test-field wavenumber $k = k_1$ and normalize the resulting α_{ij} and η_{ij} by the corresponding SOCA results in the limit of $k \rightarrow 0$:

$$\alpha_0 = -u_0^2/(2\eta k_f), \quad \eta_{10} = u_0^2/(2\eta k_f^2), \quad (28)$$

see Rheinhardt et al. (2014).

We compute $B_{\text{eq}0} = u_{\text{rms}0}\langle \rho \rangle^{1/2}$ from a simulation without external magnetic field or by virtue of Equation (12) directly from the forcing amplitude. In Figure 1 we show the diagonal components of α_{ij} and η_{ij} for Set RF1 as functions of $B_{\text{ext}}/B_{\text{eq}0}$ and also of $B_{\text{ext}}/B_{\text{eq}}$, where B_{eq} is derived from the actual u_{rms} and hence dependent on B_{ext} . The off-diagonal components are zero to high accuracy while α_{11} and α_{22} as well as η_{11} and η_{22} are very close to each other (to four digits). This apparent isotropy of the *quenched* flow is somewhat surprising as the imposed field is in general capable of introducing a new preferred direction. So let us consider the second-order change in the flow, $\mathbf{u}^{(2)}$, for

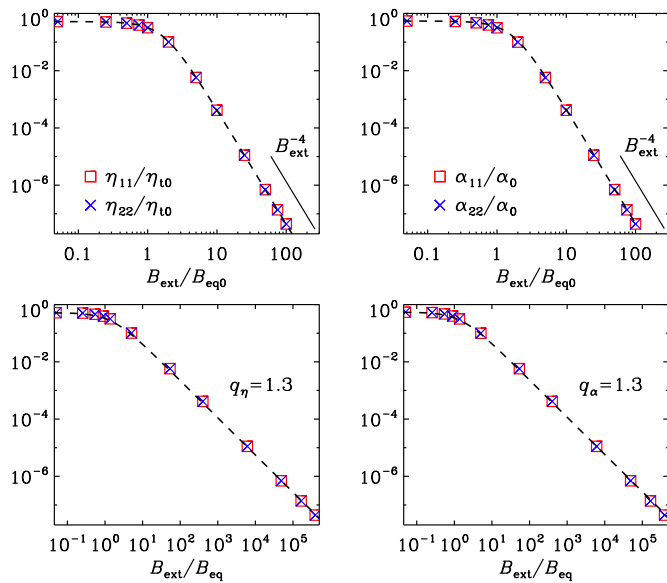


Figure 1. Results of Set RF1, $R_{m0} = 0.88$: Variations of η_{11} , η_{22} (left) and α_{11} , α_{22} (right) with the external magnetic field in the x direction. Top: dependences on $B_{\text{ext}}/B_{\text{eq0}}$ with fit (31). Bottom: dependences on $B_{\text{ext}}/B_{\text{eq}}$ with fit (32). Fits dashed.

(A color version of this figure is available in the online journal.)

small B_{ext} . From Equation (7) we get for the first-order magnetic fluctuation in the stationary case and with $R_m \ll 1$

$$\mathbf{b}^{(1)} = \frac{B_{\text{ext}}}{\eta k_0} (v_0 s x s y, v_0 c x c y, -w_0 s x c y), \quad (29)$$

and from this the solenoidal part of the second-order Lorentz force

$$\mathbf{B}_{\text{ext}} \cdot \nabla \mathbf{b}^{(1)} = \frac{B_{\text{ext}}^2}{\eta} (v_0 c x s y, -v_0 s x c y, -w_0 c x c y) \sim \mathbf{u}_0. \quad (30)$$

A quadratic contribution from $\mathbf{b}^{(1)}$ is not present as the Beltrami property $\nabla \times \mathbf{b}^{(1)} \sim \mathbf{b}^{(1)}$ holds. That is, if the Reynolds numbers (here ≤ 0.88) as well as the modification of the pressure (and thus density) by the magnetic contribution $\mathbf{b}^{(1)} \cdot \mathbf{B}_{\text{ext}}$ is small, i.e., if the corresponding plasma beta is large, the flow geometry is not changed by its second-order correction. This implies that our argument continues to hold up to arbitrary orders in B_{ext} , if only the $\mathbf{u} \cdot \nabla \mathbf{u}$ and $\nabla \times (\mathbf{u} \times \mathbf{b})'$ terms can be neglected and the pressure modification is small at any order. So for our values of R_m and Re the quenched flow differs from the original one mainly in amplitude and preserves essentially its horizontal isotropy.

The condition for Re can be relaxed when rewriting the advective terms in the second-order momentum equation in the form $(\nabla \times \mathbf{u}^{(2)}) \times \mathbf{u}_0 + (\nabla \times \mathbf{u}_0) \times \mathbf{u}^{(2)} + \nabla (\mathbf{u}^{(2)} \cdot \mathbf{u}_0)$. A solution $\mathbf{u}^{(2)} \sim \mathbf{u}_0$ can already exist (approximately), if the sum of magnetic and dynamical pressure, $\mathbf{b}^{(1)} \cdot \mathbf{B}_{\text{ext}} + \rho_0 \mathbf{u}^{(2)} \cdot \mathbf{u}_0$, is negligible compared to $p_0 = c_s^2 \rho_0$, more precisely and less restricting, if the non-constant part of this sum is negligible. At higher orders there is an increasing number of contributions to be taken into account.

Therefore, following the definition (24), we have $\alpha \approx \alpha_{11} \approx \alpha_{22}$ and $\eta_t \approx \eta_{11} \approx \eta_{22}$. The transport coefficients start to be quenched when B_{ext} exceeds B_{eq0} or B_{eq} and seem to follow a power law for strong fields. To compare with earlier works, it is

useful to consider the dependences on $B_{\text{ext}}/B_{\text{eq0}}$. Calculating the quenched coefficients under SOCA by a power series expansion with respect to B_{ext} , only the even powers occur. Accordingly, we find that our data fit remarkably well with

$$\sigma = \frac{\sigma_0}{1 + p_{\sigma 1} (B_{\text{ext}}/B_{\text{eq0}})^2 + p_{\sigma 2} (B_{\text{ext}}/B_{\text{eq0}})^4}, \quad (31)$$

where σ stands for α or η_t and $p_{\sigma 1} = 0.51$ and $p_{\sigma 2} = 0.12$; see upper panels of Figure 1. Therefore, our results are consistent with those of Sur et al. (2007) and Rheinhardt & Brandenburg (2010), who found asymptotically the power 4 for steady forcing.⁸

Alternatively, we may consider the dependences on $B_{\text{ext}}/B_{\text{eq}}$, which are weaker, because the actual B_{eq} is itself quenched. We find as an adequate model

$$\sigma = \frac{\sigma_0}{1 + p_{\sigma} (B_{\text{ext}}/B_{\text{eq}})^{q_{\sigma}}} \quad (\text{for } \sigma = \alpha \text{ or } \eta_t) \quad (32)$$

with $q_{\alpha} \approx q_{\eta} \approx 1.3$ and $p_{\alpha} \approx p_{\eta} \approx 0.59$; see lower panels of Figure 1. From now onward we shall consider the dependences on $B_{\text{ext}}/B_{\text{eq}}$ and stick to the fitting formula (32). We have performed another set of simulations with different parameters (RF2 in Table 1) and also at different wavenumbers of the test fields. In all the cases we get the same quenching behavior.

The obtained isotropy of the quenched coefficients seems to be in conflict with the results of Rheinhardt & Brandenburg (2010), who detected strong anisotropy in α_{ij} for Roberts forcing. However, the analytic consideration above makes clear, that this was a consequence of their use of a simplified momentum equation lacking the pressure term. Thus, the ingredient just necessary to allow the flow keeping its geometry while being influenced by the imposed field, was missing. One may speculate, though, that for more compressive flows the anisotropy may become visible.

4.2. Stochastically Forced Turbulence

Previous work using stochastically forced turbulence has mainly focused on α using the imposed-field method (Brandenburg et al. 1990; Cattaneo & Hughes 1996; Hubbard et al. 2009). An exception is the work of Brandenburg et al. (2008b), where α and η_t have been determined simultaneously using TFZ for super-equipartition magnetic fields resulting from saturated dynamo simulations in a triply periodic domain. Here we employ the non-helical stochastic forcing described in Section 3.1.2 with a strength adjusted such that the flow remains subsonic (Mach number ≈ 0.1). We have performed several simulations with different values of R_{m0} and with different orientations of \mathbf{B}_{ext} . Both TFZ and TFA are applied to measure the turbulent transport coefficients. For the latter we considered the requirement of gaps in the spectra of the fields (see Section 3.4.2) by choosing a high forcing wavenumber, $k_f = 27k_1$.

Due to the imperfectness of isotropy and homogeneity caused by finite scale separation of the forcing, the coefficients show fluctuations in both space and time. We usually remove them by averaging over the whole box and sufficiently long times. An exception are the coefficients α_{\perp} and α_{\parallel} that vanish on average owing to the lack of helicity, but whose fluctuations are still of

⁸ In Sur et al. (2007) a leading power of 3 is quoted, but the data in their Figure 2 are actually closer to a power of 4 as was already pointed out in Section 4.2.1 of Rheinhardt & Brandenburg (2010).

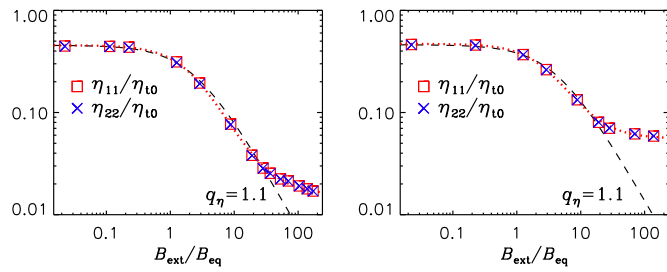


Figure 2. Dependence of η_{11} and η_{22} on the imposed field for forced turbulence; $R_{m0} = 0.87$. Left: Set TBx with $\mathbf{B}_{\text{ext}} \parallel \hat{x}$; right: Set TBz with $\mathbf{B}_{\text{ext}} \parallel \hat{z}$. Dashed lines: fits from Equation (32) with exponents q_η ; dotted lines: fits from Equation (34).

(A color version of this figure is available in the online journal.)

interest; see Section 4.2.4. As expected, and in agreement with earlier work (Brandenburg et al. 2012), γ and δ also vanish on average and are not shown here.

The time spans for temporal averaging should ideally be so long that the averages become stationary. How close we came to this is in several cases indicated by error bars showing the largest deviation of the average over any one-third of the time series from the overall average.

It is convenient to normalize the results using the unquenched and hence isotropic expression for η_i as obtained in SOCA in the high conductivity limit, i.e.,

$$\eta_{i0} = \frac{1}{3} u_{\text{rms}0} k_f^{-1}. \quad (33)$$

When we determine the fluctuations of α , we use $\alpha_0 = u_{\text{rms}0}/3$ for normalization, which would be the expected value in fully helically forced isotropic turbulence. First, we present the transport coefficients measured using TFZ, but restrict ourselves to η_{11} and η_{22} .

4.2.1. TFZ: Horizontal and Vertical Fields

Figure 2 shows the results for both horizontal and vertical external fields, $\mathbf{B}_{\text{ext}} = B_{\text{ext}} \hat{x}$ (Set TBx) and $\mathbf{B}_{\text{ext}} = B_{\text{ext}} \hat{z}$ (Set TBz); see Table 1. For these runs we have adopted $k_f/k_1 = 5$ and $\eta = \nu = 0.01 c_s/k_1$, which yields $R_{m0} = 0.87$. Note that in both cases η_{11} is almost identical to η_{22} , which is natural for the vertical field, but unexpected for the horizontal one, because η_{ij} , being an axisymmetric rank-2 tensor whose preferred direction is given by $\hat{\mathbf{B}} \parallel \mathbf{B}_{\text{ext}}$, must have the general form $\eta_{ij} = \eta_0 \delta_{ij} + \eta_1 \hat{B}_i \hat{B}_j$ with $\hat{\mathbf{B}}$ -dependent coefficients η_0 and η_1 . This has indeed been confirmed previously for a dynamo-generated $\hat{\mathbf{B}}$ of Beltrami type (Brandenburg et al. 2008b). For horizontal \mathbf{B}_{ext} we have thus $\eta_{11} = \eta_0 + \eta_1$, but $\eta_{22} = \eta_0$. The reason for the apparent vanishing of η_1 is currently unclear, but might be connected with the fact that here the field is a uniform one.

Indeed, considering a forcing, simplified such that only a single transverse (frozen) wave is supported instead of switching rapidly between waves with random wavevector and phase, one finds that a uniform imposed field of arbitrary strength does not change the geometry of that wave, but merely its amplitude, see the Appendix. Hence, for a statistical ensemble, generated by random choices of wave and polarization vectors, η_{ij} from averaging over this ensemble must remain isotropic, that is, η_1 needs to vanish. The only condition for that to hold is the negligibility of the pressure variations caused by the imposed field, compared to the pressure in the field-free

case. This finding looks similar to that obtained for the Roberts forcing case, although the mathematical reason is here the transversality of the wave flow and not its Beltrami property. Returning to the actually used delta-correlated random-wave forcing, one would conclude, that approximate isotropy could occur as long as the waves are damped quickly enough for letting their mutual interactions be subdominant. Of course, if at all, this can only happen for small Re and R_m as those in Sets TBx and TBz ($\text{Re}_0 = R_{m0} = 0.87$). With increasing Reynolds numbers, anisotropy should gradually emerge, and indeed, for $\text{Re}_0 = R_{m0} \approx 14$ we find η_{11} being by $\approx 9\%$ bigger than η_{22} when the imposed field is as weak as $B_{\text{ext}}/B_{\text{eq}} = 0.66$.

Unlike the Roberts flow case, the behavior for $B_{\text{ext}} > B_{\text{eq}}$ cannot be described by a single asymptotic power law. Instead we observe a possible transition from one power law to another one with lower power at $B_{\text{ext}} \gtrsim 20 B_{\text{eq}}$. Accordingly, the fitting formula (32), with quenching exponents $q_\eta = 1.1$ for both cases matches well only up to this value. Nevertheless in Figure 2 we see that the quenching is not exactly the same for the two field directions, namely, slightly weaker for the vertical field as we find $p_\eta = 0.21$ for the latter, but $p_\eta = 0.38$ for the horizontal field.

A satisfactory overall fit can be obtained by employing an ansatz of the form

$$\eta_{11,22}(B_{\text{ext}}) = \eta_{11,22}(0) \frac{1 + p_n(B_{\text{ext}}/B_{\text{eq}})^q}{1 + p_d(B_{\text{ext}}/B_{\text{eq}})^q} \quad (34)$$

with $q = 1.36$ and 1.31 for horizontal and vertical field, respectively; see the red dotted lines in Figure 2. This can be taken as an indication of asymptotic independence of $\eta_{11,22}$ on B_{ext} , which makes sense as the turbulence should asymptotically become two-dimensional with $\mathbf{B}_{\text{ext}} \cdot \nabla \mathbf{u} = \mathbf{0}$. Note that we do not observe this in the Roberts forcing case because there, as demonstrated above, the flow has no freedom to adjust to this condition, at least for not too high R_m .

If we normalize B_{ext} in Equation (32) by $B_{\text{eq}0}$, the scaling changes and the exponent q_η becomes 1.5 and 1.4 for horizontal and vertical external fields, respectively. These values are higher than the result of Kitchatinov et al. (1994) and Rogachevskii & Kleeorin (2001), who found unity.

When comparing the two panels of Figure 2 one might ask why the quenching characteristics of η_{22} for horizontal and vertical \mathbf{B}_{ext} are not identical although this coefficient is in both cases correlating components of $\hat{\mathbf{E}}$ and $\hat{\mathbf{J}}$ perpendicular to the preferred direction. This apparent ambiguity can be resolved with a view to Equation (5): Provided that $\epsilon \approx 0$ (which will be demonstrated in the next section), we have for vertical external field $\nabla = \nabla_\parallel \hat{e}_z$, hence η_i and μ sum up, while for horizontal \mathbf{B}_{ext} of course $\nabla_\parallel = 0$, so $\eta_{11}(= \eta_{22})$ should differ in the two cases roughly by μ . That is, the anisotropy of the turbulence does manifest in the diffusive behavior, but not by causing an anisotropic η_{ij} .

4.2.2. TFA: Determining Anisotropy

To measure the anisotropy of turbulent diffusion, we have applied TFA for axisymmetric turbulence whose preferred direction is defined by the imposed field. Hence, we consider the case $\mathbf{B}_{\text{ext}} = B_{\text{ext}} \hat{z}$. We measure all the relevant transport coefficients described in Equation (4). Here we only show η_\perp , η_\parallel , and μ . It turns out that κ_\perp and κ_\parallel are negative (around -0.01 in units of η_{i0}) for our largest field strengths, but zero within error bars for weaker fields and hence not shown. All other

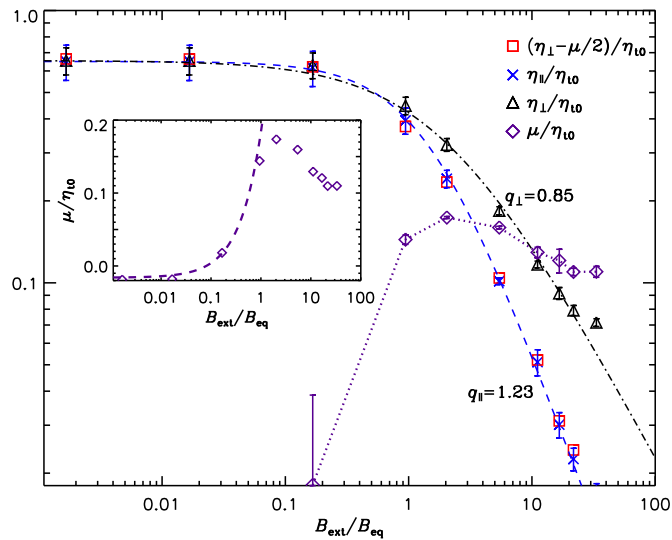


Figure 3. Results of Set AT1, $R_{m0} = 2.23$. Variation of η_{\parallel} (crosses), η_{\perp} (triangles), μ (diamonds, dotted), and $\eta_{\perp} - \mu/2$ (squares), all normalized by η_{i0} , with the imposed field $B_{\text{ext}}/B_{\text{eq}}$; dashed and dash-dotted: fits to η_{\parallel} and η_{\perp} , respectively, from Equation (32). Dashed line in inset: linear fit with slope 0.2. (A color version of this figure is available in the online journal.)

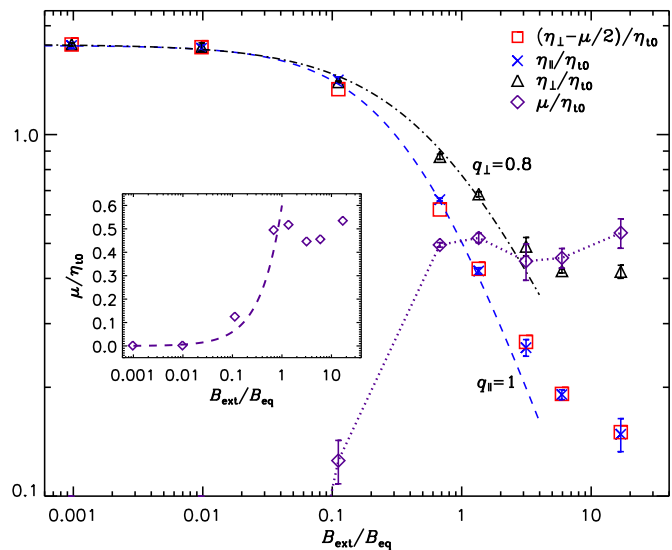


Figure 4. As Figure 3, but for Set AT2, $R_{m0} = 18.2$ and the linear fit (dashed line in inset) has slope 0.6 here. (A color version of this figure is available in the online journal.)

coefficients are at least about 10 times smaller and fluctuating about zero; see Section 4.2.4 for some discussion about those fluctuations. We denote this set of simulations by AT1 and show its results in Figure 3; see also Table 1. It turns out that η_{\perp} is less strongly quenched than η_{\parallel} . According to the fitting formula (32), we have $q_{\parallel} = 1.2$, but $q_{\perp} = 0.85$. The coefficient μ is increasing with B_{ext} until a maximum at $B_{\text{ext}}/B_{\text{eq}} \approx 2$. Interestingly, we have $\eta_{\parallel} \approx \eta_{\perp} - \mu/2$; see red squares in Figure 3. If we apply this finding in Equation (5) we see that because of $\epsilon \approx 0$ the mean-field induction equation takes the simple form $\partial_t \bar{\mathbf{B}} = ((\eta + \eta_{\perp} - \mu/2)\nabla^2 + \mu\nabla_{\parallel}^2)\bar{\mathbf{B}}$. We may redefine the preferred direction to coincide now with $\hat{\mathbf{x}}$ and assume at the same time, that all mean quantities depend solely on z , hence $\nabla_{\parallel} = 0$. In this way we can make contact with the results of TFZ for horizontal fields arriving at $\eta_{11} = \eta_{22} = \eta_{\perp} - \mu/2$. So

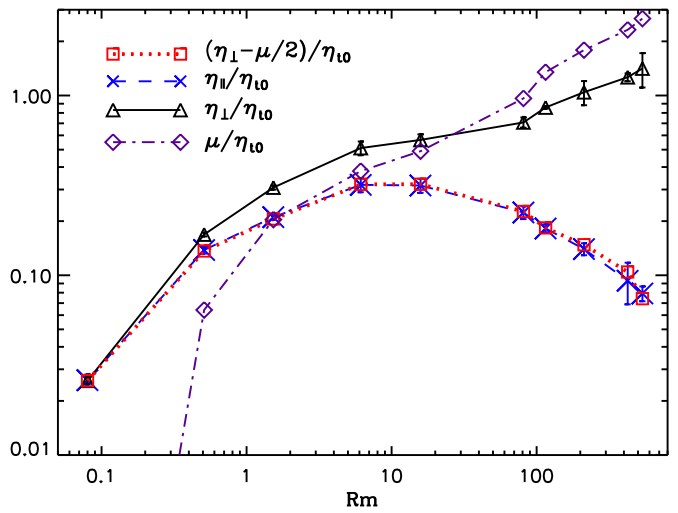


Figure 5. R_m dependence of the turbulent diffusivity in axisymmetric turbulence with a fixed $B_{\text{ext}}/B_{\text{eq}} \approx 4.3$ (Set AT3). Squares: $\eta_{\perp} - \mu/2$; crosses: η_{\parallel} ; triangles η_{\perp} ; diamonds: μ , all normalized by η_{i0} . (A color version of this figure is available in the online journal.)

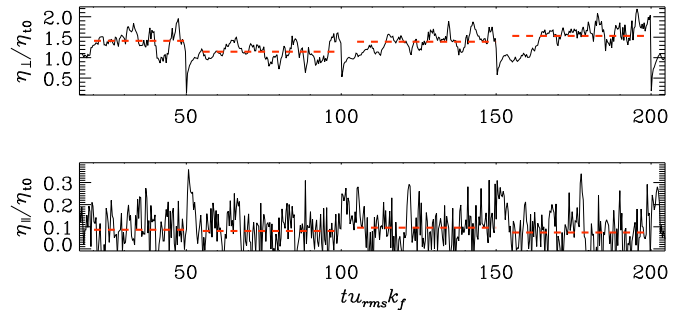


Figure 6. Small portion of the time series of z -averaged η_{\perp} and η_{\parallel} for the highest $R_m = 537$ (from Set AT3) with imposed field $B_{\text{ext}}/B_{\text{eq}} \approx 4.3$. Time is normalized by the turnover time $(u_{\text{rms}} k_f)^{-1}$. Dashed lines: averages over the resetting intervals. We take the average of many (≥ 10) such intervals. (A color version of this figure is available in the online journal.)

the somewhat surprising *isotropy* of η_{ij} obtained with TFZ is confirmed with TFA in spite of $\eta_{\perp} \neq \eta_{\parallel}$.

4.2.3. R_m Dependence

To study the influence of R_m , we performed simulations with the higher value $R_{m0} = 18.2$; see Set AT2 in Table 1. Figure 4 shows that for this set the quenching exponents of η_{\perp} and η_{\parallel} are reduced mildly. The μ increases more rapidly with B_{ext} compared to Set AT1 and seems to saturate at large fields. Moreover, we have performed simulations with a fixed value of $B_{\text{ext}}/B_{\text{eq}} \approx 4.3$, but R_m increasing from 0.07 to 537; see Figure 5. For the largest values of R_m , the resetting of the test solutions (see Section 3.4) is most critical, but it turns out that the resulting values of η_{\perp} and η_{\parallel} show clear plateaus where statistically stable averages can be taken; see Figure 6 for an example.

At low R_m we do not see much anisotropy, but for $R_m > 1$, η_{\perp} becomes significantly larger than η_{\parallel} . Interestingly, at about $R_m = 10$, η_{\parallel} reaches a maximum, whereas η_{\perp} increases even at the largest R_m , as does μ . We find again that $\eta_{\perp} - \mu/2$ is almost identical to η_{\parallel} .

It has been reported earlier that in forced hydrodynamic turbulence η_t increases linearly with R_m at smaller values and saturates beyond $R_m \approx 10$ (Sur et al. 2008). However this

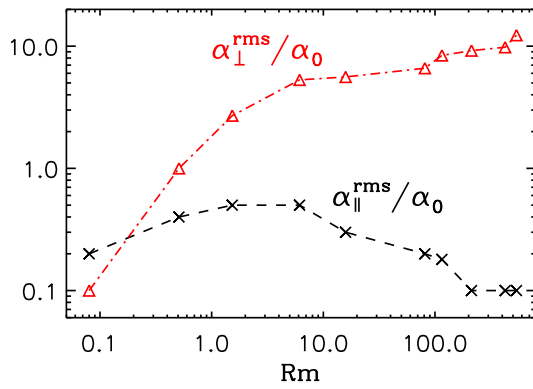


Figure 7. As Figure 5, but showing the fluctuations of α as functions of R_m . Crosses: $\alpha_{\parallel}^{\text{rms}}$; triangles: $\alpha_{\perp}^{\text{rms}}$.

(A color version of this figure is available in the online journal.)

is not so in our hydromagnetic turbulence. Unfortunately, the instability of the test problems for high R_m prevents us from looking further for a possible saturation.

4.2.4. Incoherent α Effect

For non-helical isotropic forcing, the α tensor vanishes on average when rotation or stratification is absent. As emphasized by Brandenburg et al. (2008a), however, its fluctuations, also referred to as “incoherent α effect,” may in general have relevance for dynamo processes, especially if they interact with large-scale shear (Vishniac & Brandenburg 1997; Heinemann et al. 2011; Mitra & Brandenburg 2012). In our simulations they are too weak to lead to self-excitation though. In Figure 7 we show the volume-averaged temporal fluctuations of α_{\perp} and α_{\parallel} as functions of R_m in terms of their rms values, defined as $\langle \alpha_{\perp}^2 \rangle_t^{1/2}$ and $\langle \alpha_{\parallel}^2 \rangle_t^{1/2}$, respectively, where the subscript t refers to time averaging. While $\alpha_{\perp}^{\text{rms}}$ increases with R_m , $\alpha_{\parallel}^{\text{rms}}$ increases only slightly at moderate R_m , but decreases beyond $R_m \approx 5$. Fluctuations in z could also be important and would increase the rms values of α_{\perp} and α_{\parallel} but have been ignored here.

4.3. Stratified Convection

Finally, we turn to convection, in which already in the absence of a magnetic field a preferred direction is set by gravity and thus density stratification. All the relevant transport coefficients are measured using TFZ with wavenumber $k = k_1$, except that in one case we also consider $k = 0$. As in the case of homogeneous forced turbulence, we present time-averaged results, but owing to the intrinsic inhomogeneity of the setup, no z averaging is performed by default. Error bars are generated as described for forced turbulence.

In deriving quenching characteristics for an inhomogeneous turbulence from numerical experiments with an imposed (uniform) field, one has to remember that the actually quenching mean field needs not coincide with the imposed one. In general, as a consequence of Equation (1), a mean electromotive force is caused by \mathbf{B}_{ext} , which in turn can give rise to an additional constituent of \mathbf{B} . This could of course not happen in our setups with forcing, as there the generated \mathbf{E} is uniform. For convection, however, the transport coefficients are at least z dependent (for TFZ) and the x and y components of \mathbf{E} will result in $\mathbf{B} \neq \mathbf{B}_{\text{ext}}$ due to the generation of one or even two components orthogonal to \mathbf{B}_{ext} . For horizontal \mathbf{B}_{ext} the imposed content itself is also modified.

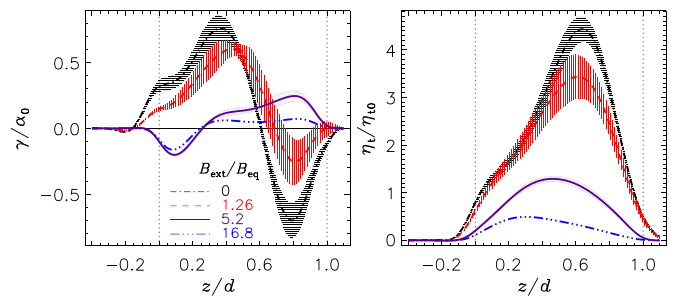


Figure 8. Dependences of γ (left) and η_t (right) on the vertical coordinate z for different $B_{\text{ext}}/B_{\text{eq}}$ (Set CR0). Hatched areas: errors (not shown for $B_{\text{ext}}/B_{\text{eq}} = 16.8$ as indistinguishable from the mean). Dotted lines at $z = 0, 1$: boundaries of the convectively unstable region.

(A color version of this figure is available in the online journal.)

4.3.1. Non-rotating Convection

First, we present results for the simplest situation without rotation or large-scale shear (Set CR0, listed in Table 1). No (coherent) α effect is expected, but turbulent pumping, i.e., a γ effect, should occur due to the inhomogeneities caused by stratification and boundaries. Figure 8 presents profiles of γ and η_t for four different values of the imposed magnetic field B_{ext} from zero to $\approx 17B_{\text{eq}}$. We see that the unquenched profiles of γ and η_t are similar to what has been found by Käpylä et al. (2009a) and that even when $B_{\text{ext}}/B_{\text{eq}} \gtrsim 1$, at least η_t is not quenched much. However, for $B_{\text{ext}}/B_{\text{eq}} > 2$, both γ and η_t are suppressed significantly, and γ is even changing sign. Moreover, the level of fluctuations is markedly reduced at the highest $B_{\text{ext}}/B_{\text{eq}}$ and the convection itself is suppressed to the extent that it only shows elongated cells; see Table 1 for the reduction of u_{rms} (cf. R_m). This is a consequence of our choice of using relatively small values of R_m and Re , with the effect that the convection is only mildly supercritical and therefore more vulnerable to quenching.

For weak and moderately strong fields, negative (positive) values of γ are seen in the upper (lower) part of the domain, which corresponds to downward (upward) pumping, i.e., toward the middle of the convection zone. These directions are just opposite to what analytic theory predicts for *uniform* mean fields, namely, that the pumping is directed away from the maximum of the turbulence intensity. The obtained behavior agrees, however, with the findings of Käpylä et al. (2009a) for harmonic test fields with $k = k_1$ which are also employed in this section. For stronger fields the sign is reversed, as expected for magnetic buoyancy (Kitchatinov & Pipin 1993). In Section 4.3.3 we will show results for uniform test fields ($k = 0$) and compare them with the theoretical prediction.

The coefficients are intrinsically z dependent, but for the sake of clarity in presenting their dependences on B_{ext} , we calculate the averages of $\eta_{11,22}$ and $|\gamma|$ over a certain z extent, typically $0.2 \leq z/d \leq 0.9$. Other intervals or even the degenerate case of fixed values of z , however, yield very similar quenching behaviors. In Figure 9, we present $\eta_{11,22}$ and γ , averaged in this way, in dependence on B_{ext} . Fitting the data with the formula (32), we find $q_{\gamma,\eta} = 1.2$, which is very close to our earlier results for the Roberts flow, but slightly larger than those found in forced turbulence. Finding the same quenching dependence of γ and η_t seems sensible in light of the result of the linear theory of Roberts & Soward (1975), $\gamma = -\partial_z \eta_t / 2$. When we normalize B_{ext} with $B_{\text{eq}0}$ we find for the exponents $q_{\gamma,\eta} \approx 2.2$. The value of q_{γ} disagrees with the

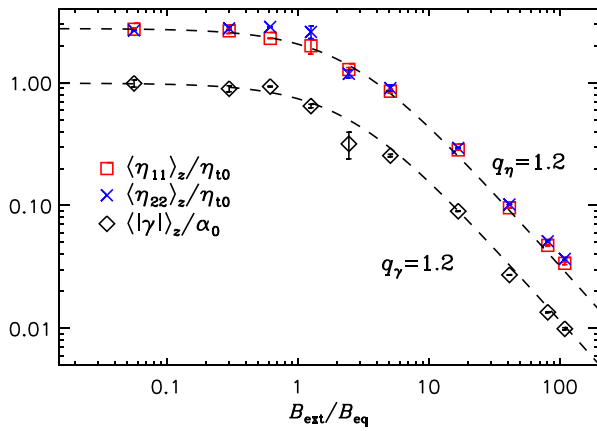


Figure 9. Results from Set CR0: Dependences of $\langle \eta_{11} \rangle_z$ (squares) $\langle \eta_{22} \rangle_z$ (crosses) and $\langle |\gamma| \rangle_z$ (diamonds) on $B_{\text{ext}}/B_{\text{eq}}$. Dashed lines: fits from formula (32) with exponents $q_{\eta,\gamma} = 1.2$.

(A color version of this figure is available in the online journal.)

analytical result of Rogachevskii & Kleeorin (2006). However, this was derived for turbulent pumping being caused by the density gradient, which can hardly be dominant here because of weak density stratification. Therefore, our result is closer to the exponent 2 that is found when pumping is caused by a gradient in the turbulence intensity instead (see Section 4.3.3 for the validation).

4.3.2. Rotating Convection

Next we consider rotating convection with the rotation axis aligned along the z direction ($\theta = 0$), whereas the magnetic field is along the x direction. We expect an α -effect because $\mathbf{g} \cdot \boldsymbol{\Omega} \neq 0$. Figure 10 shows the profiles of the measured transport coefficients at different strengths of the external field with α_{ij} normalized to the isotropic value for maximum helicity $\alpha_0 = u_{\text{rms}0}/3$ and η_{ij} normalized to η_{t0} (see Eq. (33)). The main diagonal elements of both tensors are for $B_{\text{ext}} \neq 0$ not equal because the external field is applied along the x direction. For vanishing and weak B_{ext} , both α_{11} and α_{22} change sign, albeit not at exactly the same position; they are then positive in (roughly) the upper half of the convective zone and negative in the lower one, again consistent with earlier findings of Ossendrijver et al. (2001) and Käpylä et al. (2009a). Importantly, α_{11} decreases rapidly with increasing B_{ext} . However, α_{22} increases at first and only later decreases.

The components $\eta_{11,22}$ have very similar profiles not only for vanishing, but also for very strong magnetic field, differing a bit more for intermediate field strengths. The off-diagonal components of the η tensor are here of interest mainly in the combination $\delta = (\eta_{21} - \eta_{12})/2$, which characterizes the $\boldsymbol{\Omega} \times \mathbf{J}$ effect. In agreement with earlier work for rotating convection (Käpylä et al. 2009a), the sign of δ is mainly positive, while for rotating forced turbulence, Brandenburg et al. (2008a, 2012) found it to be negative. It is also remarkable that δ is only mildly quenched unless the magnetic field becomes very strong. We further see that $\eta_{21} + \eta_{12}$ is not small. This quantity would vanish in the absence of a magnetic field, but it is apparently quite sensitive even to weak fields.

The lowermost panels in Figure 10 show the mean kinetic and current helicity as defined by $\bar{h}_k = \overline{\boldsymbol{\omega} \cdot \mathbf{u}}$ with $\boldsymbol{\omega} = \nabla \times \mathbf{u}$, and $\bar{h}_c = \overline{\mathbf{j} \cdot \mathbf{b}}$, respectively. For weak fields, the kinetic helicity is positive in the lower third and negative in the upper two thirds of the unstable layer, while the current helicity changes

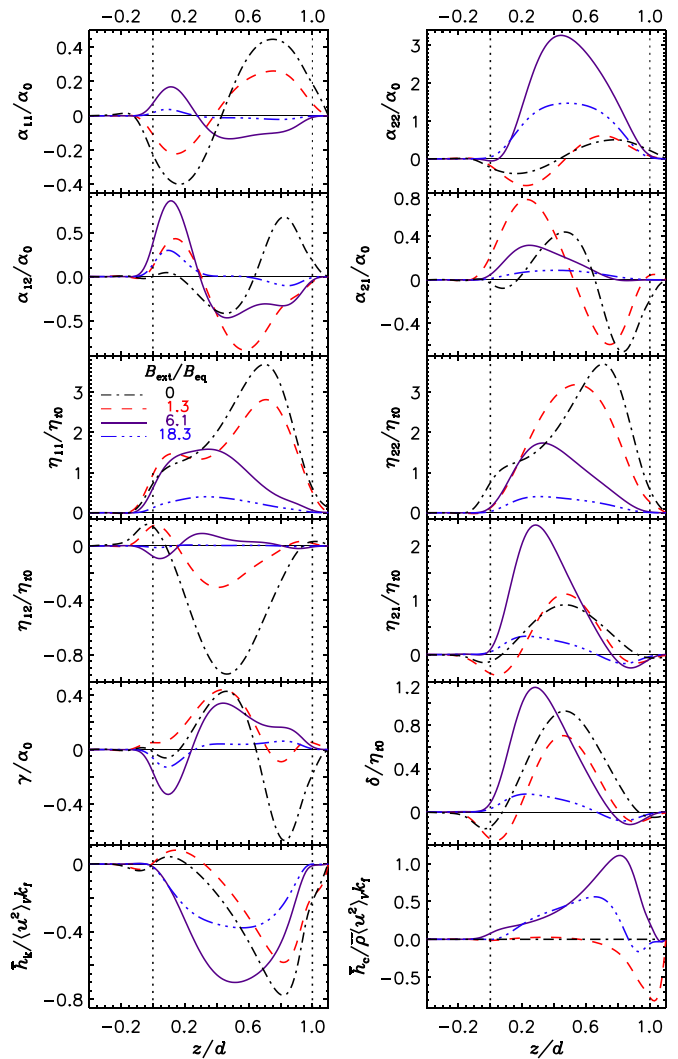


Figure 10. Results from Set CR1: variations of α_{ij} , η_{ij} , γ , δ , and the mean kinetic and current helicity, \bar{h}_k and \bar{h}_c , respectively, along the vertical coordinate z at different field strengths. \bar{h}_k and \bar{h}_c are normalized by $\langle \mathbf{u}^2 \rangle_V k_f$ and $\overline{\rho} \langle \mathbf{u}^2 \rangle_V k_f$, respectively, where $\langle \cdot \rangle_V$ indicates volume averaging. Dotted lines at $z/d = 0, 1$: boundaries of the convectively unstable region.

(A color version of this figure is available in the online journal.)

from positive to negative only at $z \approx 0.6d$. So the expectation of sign equality of the helicities, nourished by ideas of α quenching originating from closure approaches (Pouquet et al. 1976; Kleeorin & Ruzmaikin 1982), is only very roughly met. For strong fields, however, both helicities show only one sign, opposite to each other, over almost the entire domain. The current helicity increases first rapidly with the imposed field, but for the strongest fields both helicities begin to be quenched.

In Figure 11, showing the absolute values of the transport coefficients averaged over $0.2 \leq z/d \leq 0.9$, we find $\langle |\alpha_{11}| \rangle_z$ being quenched according to Equation (32) with $q_{\alpha_{11}} = 1.8$. By contrast, $\langle |\alpha_{22}| \rangle_z$ is growing until $B_{\text{ext}}/B_{\text{eq}} \approx 6$, where it reaches roughly eight times its unquenched value, and is falling then, but with a lower power than $\langle |\alpha_{11}| \rangle_z$, namely, $q_{\alpha_{22}} \approx 1$. Similarly to the α quenching for Roberts forcing, we find that the quenching exponents are larger when normalizing by $B_{\text{eq}0}$: about 3 for $\langle |\alpha_{11}| \rangle_z$ and asymptotically perhaps about 2 for $\langle |\alpha_{22}| \rangle_z$. The power 3 agrees with earlier analytic results of Moffatt (1972), Rüdiger (1974), and Rüdiger & Kitchatinov (1993), while the

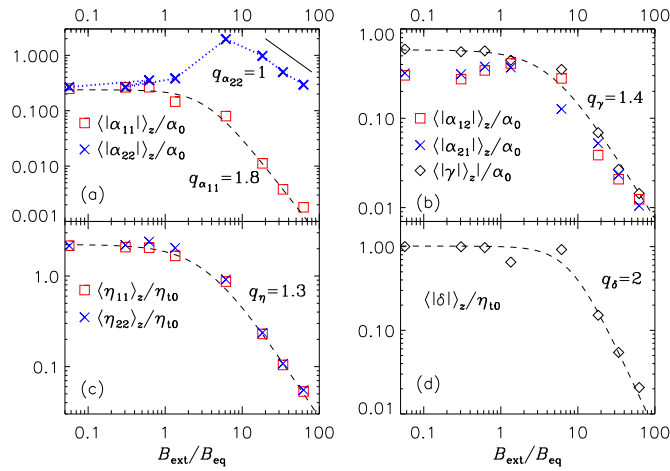


Figure 11. Results from Set CR1: variations of (a) $\langle \alpha_{11,22} \rangle_z$, (b) $\langle \alpha_{12,21} \rangle_z$, $\langle \gamma \rangle_z$, (c) $\langle \eta_{11,22} \rangle_z$, and (d) $\langle \delta \rangle_z$ with the external field. Dashed lines: fits from Equation (32).

(A color version of this figure is available in the online journal.)

power 2 agrees with the exponent found by Rogachevskii & Kleeorin (2000), who all normalized by B_{eq0} .

The quantities $\langle \eta \rangle_z$ and $\langle \gamma \rangle_z$ show also systematic quenching with exponents very similar to those found earlier in non-rotating convection ($q = 1.2$) and in fact identical to the results for Roberts forcing ($q = 1.3$). As we have rotation, another relevant quantity is δ , defined in Equation (24), which is essential for the $\Omega \times J$ dynamo in non-helical turbulence with shear, cf. Equation (4). For a recent application to stellar dynamos see Pipin & Seehafer (2009). Figure 11 shows the variation of $\langle \delta \rangle_z$ with B_{ext} , and we find strong quenching with $q_\delta = 2$.

As mentioned above, for the inhomogeneous turbulence in convection we must take into account that $\bar{B} \neq B_{ext}$. Therefore, we show in Figure 12 for Set CR1 (cf. Figure 11), how the transport coefficients are quenched with the local $\bar{B}(z)/B_{eq}(z)$. For comparison, the fit to the z averaged quantities from Equation (32) is shown by the dashed lines. A more appropriate representation is obtained by considering the turbulent transport coefficients as functions of both the local $\bar{B}(z)$ and $R_{m0}(z)$, as they should also depend on the intrinsic (unquenched) local strength of the turbulence. This view is provided in Figure 13, where the arguments in the $(\bar{B}/B_{eq}, R_{m0})$ plane were formed by taking both quantities from the same set of z positions within the convection zone for eight different values of B_{ext} . The shown surface was then obtained by linear interpolation over a Delaunay triangulation of the irregularly spaced arguments. In $\eta_{11,22}$ we see for fixed R_{m0} the common power-law quenching behavior, while the dependence on R_{m0} for fixed \bar{B}/B_{eq} grows until saturation for small $\bar{B}/B_{eq} \lesssim 5$, but falling beyond. $|\alpha_{11}|$ shows a similar power-law behavior with \bar{B}/B_{eq} for fixed R_{m0} , but there is in general a sign change of α_{11} for \bar{B}/B_{eq} between 1 and 10. At best, a very narrow R_{m0} interval exists without sign change. As already indicated by Figure 11, the behavior of $|\alpha_{22}|$ is different in that it is first growing with \bar{B}/B_{eq} reaching a maximum at ≈ 5 for all values of R_{m0} . As a remarkable feature we see a sign change only up to $\bar{B}/B_{eq} \gtrsim 3$. Beyond, the R_{m0} dependence is becoming weak with a flat maximum.

It remains open, whether the transport coefficients are really local functions of the two quantities employed, or whether there is also a generic dependence on the local mean current density. In addition, non-locality of turbulent transport has

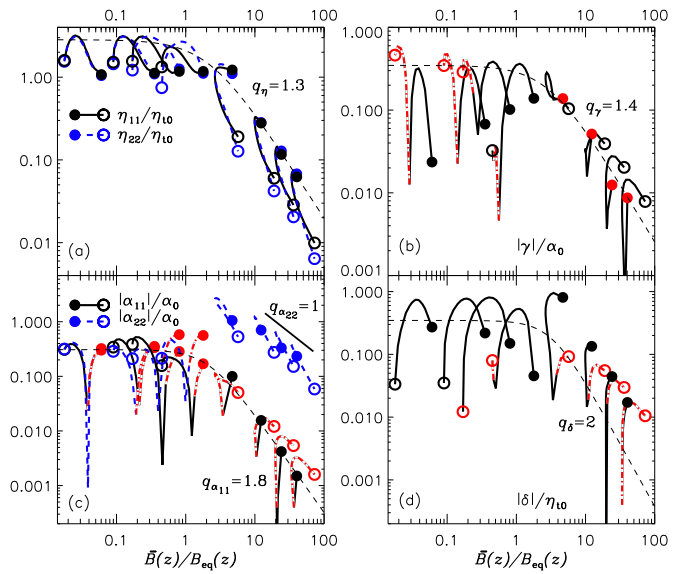


Figure 12. As Figure 11 from Set CR1, but all coefficients are computed locally at 14 equidistant z positions, $0.2d \leq z \leq 0.9d$, in the convective zone and are plotted against the local value of $\bar{B}(z)/B_{eq}(z)$. Each curve, limited by filled and open circles, corresponds to one of the values of $B_{ext}/(B_{eq0}(z))_z$ out of 0.21, 0.83, 2.1, 4.1, 10.3, 20.7, 31.0, and 41.3, in the order of increasing \bar{B}/B_{eq} -positions of filled circles (but not necessarily of open circles). Filled and open circles refer to $z/d = 0.2$ and $z/d = 0.9$, respectively, thus z is the curve parameter. Dashed lines: fits to the z averaged quantities from Equation (32). Dash-dotted curve sections in (b), (c), and (d) indicate negative γ , $\alpha_{11,22}$ and δ .

(A color version of this figure is available in the online journal.)

been ignored throughout, which is only permissible at large enough scale separation; see Rheinhardt & Brandenburg (2012). Note that the dependences on \bar{B}/B_{eq} and R_{m0} were entangled in the result of Brandenburg et al. (2008b) as there \bar{B} , being dynamo generated, could not be varied independently of R_{m0} .

In another set of simulations, the external field is applied along the vertical direction; see Set CR1Bz in Table 1. Figure 14 shows the dependences of $\langle \alpha_{11,22} \rangle_z$ on the external field. We see that $\langle \alpha_{11} \rangle_z$ is very close to $\langle \alpha_{22} \rangle_z$, but now both are quenched with the exponent $q_\alpha = 1.3$, which is smaller than the one of $\langle \alpha_{11} \rangle_z$ for horizontal external field; see Set CR1. Unlike in that case, $\langle \alpha_{22} \rangle_z$ shows no “anti-quenching”; cf. Figure 11. For $\langle \eta \rangle_z$ and $\langle \gamma \rangle_z$, the quenching exponents are equal to those for the horizontal field case, but for $\langle \delta \rangle_z$ we get $q_\delta = 1.8$ instead of 2. To confirm these findings, we have repeated the simulations at higher Ra and R_m and find similar results; see Set CR3Bz in Table 1.

4.3.3. Turbulent Pumping for Uniform Test Fields

According to analytic SOCA theory, developed for uniform (or linear) mean fields, turbulent pumping is related to the inhomogeneity of the turbulence through (Krause & Rädler 1980)

$$\gamma_{SOCA} = -(\tau_\gamma/2)\partial_z \overline{u_z^2}, \quad \tau_\gamma \approx \tau_{corr}. \quad (35)$$

Hence, we now employ TFZ with *uniform* test fields ($k = 0$) in the sets CR6 and CR7 having horizontal imposed field, see Table 1. Figure 15 shows the z profiles of γ for different values of B_{ext} together with those of γ_{SOCA} where τ_{corr} has been set to the (z dependent) mixing-length estimate $H_p/\langle \overline{u^2} \rangle_t^{1/2}$. Comparison reveals that for $B_{ext} = 0$ there is sign agreement of γ and γ_{SOCA} only close to the bottom of the convection zone. However,

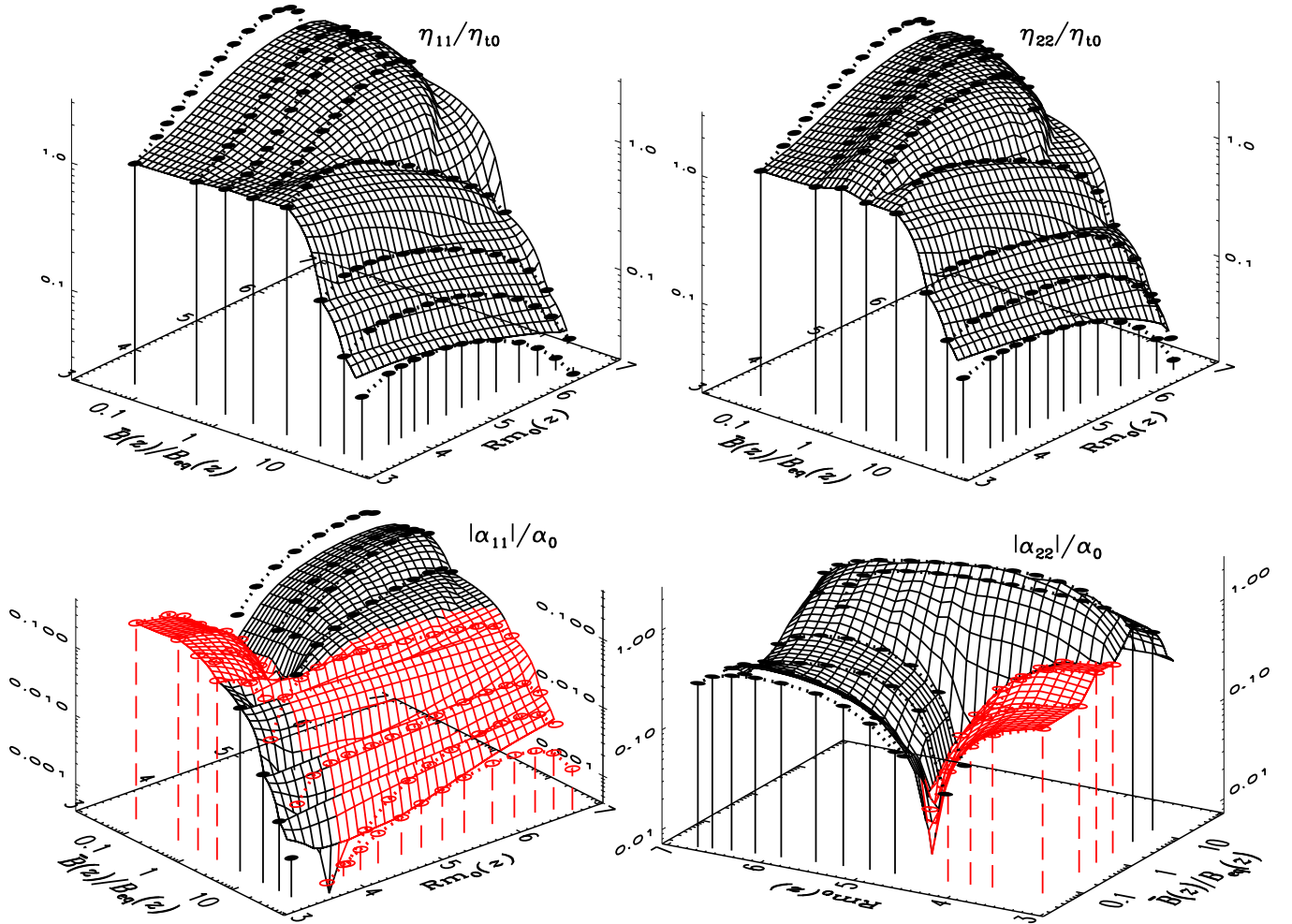


Figure 13. As Figure 12 (Set CR1), but coefficients shown as functions of \bar{B}/B_{eq} and R_{m0} , both depending on z . Upper panels: η_{11} and η_{22} ; lower panels: $|\alpha_{11}|$ and $|\alpha_{22}|$. Circles: data points, solid/open–positive/negative. Surface: linear interpoland over a triangular grid. Dotted lines connect points which belong to the same $B_{\text{ext}}/(B_{\text{eq}0}(z))_z$. Colors: black/red–positive/negative.
(A color version of this figure is available in the online journal.)

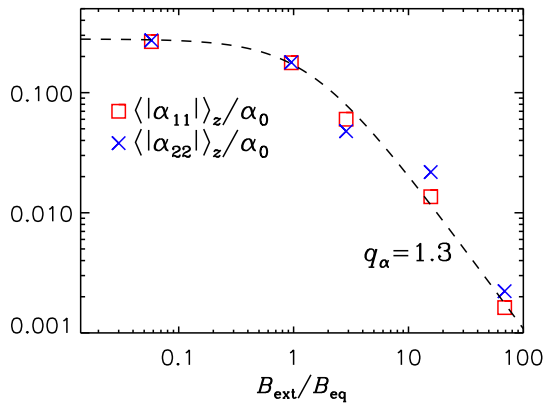


Figure 14. Results from Set CR1Bz for $B_{\text{ext}} \parallel \hat{z}$: variation of $\langle |\alpha_{11}| \rangle_z$ (squares) and $\langle |\alpha_{22}| \rangle_z$ (crosses) with $B_{\text{ext}}/B_{\text{eq}}$; cf. Figure 11 for Set CR1.
(A color version of this figure is available in the online journal.)

already at $B_{\text{ext}}/B_{\text{eq}} = 1.3$ the signs match rather well and do so perfectly at $B_{\text{ext}}/B_{\text{eq}} = 18.3$. The lack of quantitative agreement in the last two cases can most likely be assigned to the crude estimate of τ_γ . In the unquenched case, by contrast, no complete agreement can be expected since SOCA is no longer reliable

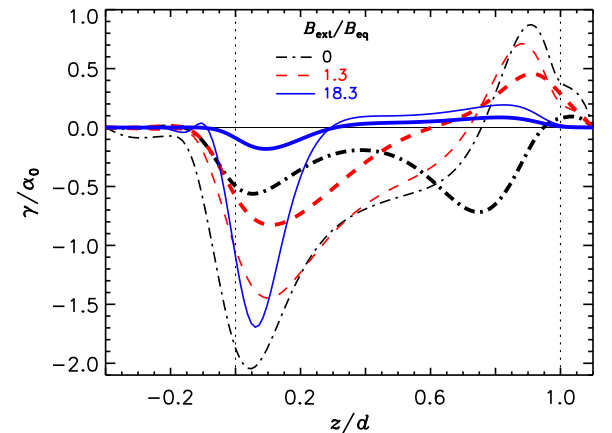


Figure 15. Results of Set CR6: as Set CR1, but for uniform test fields. Thick lines: TFZ results for $B_{\text{ext}}/B_{\text{eq}} = 0, 1.3$ and 18.3 ; Thin lines: corresponding profiles of γ_{SOCA} , see Equation (35).
(A color version of this figure is available in the online journal.)

at $R_m = R_{m0} = 3.85$, whereas the quenched values of R_m approach the validity range of SOCA again. For $B_{\text{ext}} \gg B_{\text{eq}}$, we see that γ is strongly quenched, in particular in the upper

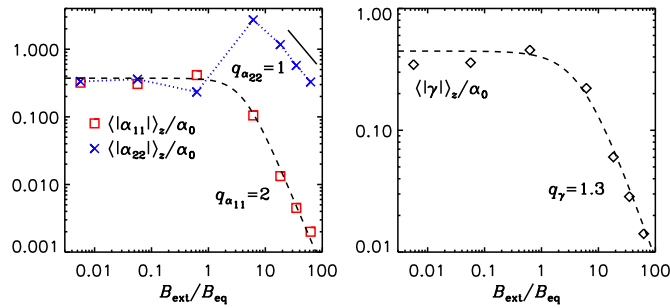


Figure 16. Results of Set CR6: as Figure 11 (Set CR1), but for uniform test fields.

(A color version of this figure is available in the online journal.)

two-thirds of the convective region. A comparison with Figure 8 confirms the strong sensitivity of γ – even in sign – with respect to the test-field wavenumber, noticed already in Käpylä et al. (2009a). Only for the highest $B_{\text{ext}}/B_{\text{eq}}$ there is some agreement of the γ profiles for $k = 0$ and $k = k_1$.

In Figure 16, we present the magnetic field dependences of $\langle |\gamma| \rangle_z$ and $\langle |\alpha_{11,22}| \rangle_z$, which are similar to what was found in Set CR1 for z -dependent test fields; cf. Figure 11. Set CR7 with higher R_m yields essentially the same results.

5. CONSEQUENCES FOR MEAN-FIELD DYNAMOS

One of the ultimate goals of our work is the application of the numerically obtained quenching functions to mean-field dynamos that can be validated by comparison against turbulence simulations and that can perhaps eventually be extrapolated to solar and stellar regimes. One of our striking results that might have consequences when applied to mean-field models is the fact that for isotropically forced turbulence the value of μ keeps increasing with R_m and exceeds η_t by more than a factor of two when $B_{\text{ext}} \gtrsim 10B_{\text{eq}}$. So turbulent diffusion is enhanced in the direction of the magnetic field relative to that in the perpendicular direction (cf. Equation (5)), but note that η_t is quenched by an order of magnitude and more at such strong B_{ext} . Furthermore, in Equation (5), ϵ is negligible compared with η_t , and so are κ_\perp and κ_\parallel . Thus, the dynamo equation takes the form

$$\partial \bar{\mathbf{B}} / \partial t = \nabla \times (\alpha \cdot \bar{\mathbf{B}}) + \eta_T \nabla^2 \bar{\mathbf{B}} + \mu \nabla_\parallel^2 \bar{\mathbf{B}}, \quad (36)$$

where an (anisotropic) α effect has been added.

It is important to note that anisotropic diffusion acts here differently from what is sometimes assumed in axisymmetric dynamo models (Chatterjee et al. 2004; Jiang et al. 2007; Yeates et al. 2008; Karak & Choudhuri 2011, 2012, 2013). To clarify this, let us assume that \hat{z} is the toroidal direction and that the toroidal field is dominating, implying $\hat{e} = \hat{z}$ and $\nabla_\parallel = 0$, while x and y are coordinates in the meridional plane. We can then write the magnetic field as

$$\bar{\mathbf{B}}(x, y, t) = \nabla \times (\hat{z} \bar{A}_\parallel) + \hat{z} \bar{B}_\parallel, \quad (37)$$

and, using this in Equation (3) with Equation (4), but γ , δ , κ_\parallel , and κ_\perp neglected, we get (cf. Bykov et al. 2013)

$$\partial \bar{A}_\parallel / \partial t = \alpha_A \bar{B}_\parallel + \eta_A \nabla^2 \bar{A}_\parallel, \quad (38)$$

$$\partial \bar{B}_\parallel / \partial t = \alpha_B \bar{B}_\parallel + \eta_B \nabla^2 \bar{B}_\parallel, \quad (39)$$

where

$$\alpha_A = \alpha_\parallel, \quad \alpha_B = \alpha_\perp, \quad (40)$$

$$\eta_A = \eta + \eta_\parallel, \quad \eta_B = \eta + \eta_\perp - \mu/2. \quad (41)$$

With $\eta_\parallel \approx \eta_\perp - \mu/2$, however, $\eta_A \approx \eta_B$ holds, hence the diffusion is actually isotropic. As alluded to above, this is in contrast to previously adopted reasoning by which η_A should be much larger than η_B (e.g., Chatterjee et al. 2004; Jiang et al. 2007; Yeates et al. 2008; Karak & Choudhuri 2011). We have to stress, however, that the isotropy we found may well be an artifact of the rather specific way of forcing turbulence by transverse waves.

Furthermore, the amount of quenching assumed in some mean-field models is rather large, for example, Muñoz-Jaramillo et al. (2011) employed a reduction of the magnetic diffusivity by nearly two orders of magnitude in the lower half of the convection zone compared to the mixing length estimate. According to our results, this would require field strengths that exceed the equipartition value correspondingly also by two orders of magnitude. In most of the solar convection zone the equipartition value B_{eq0} is around 5000 G (see Stix 2002), so the mean field strength required for such strong quenching would have to reach the unlikely order of several 10^5 G at the bottom.

Although several mean-field dynamo models (e.g., Brandenburg et al. 1992; Käpylä et al. 2006; Guerrero & de Gouveia Dal Pino 2008; Do Cao & Brun 2012; Karak & Nandy 2012; Pipin & Kosovichev 2014) include turbulent pumping, its quenching is usually ignored. As an exception, Käpylä et al. (2006) include quenching of γ with exponent 2 in a formulation with respect to B_{eq0} , which is close to ours with a value of about 2.3.

The question now is to what extent our new results can be used in modeling the mean magnetic field evolution either in turbulence simulations of convectively driven dynamos or even in the Sun. In recent years, simulations have displayed a wealth of different behaviors that are hard to explain with our current knowledge. Examples include the equatorward migration in the simulations of Käpylä et al. (2012), which is only found in the saturated regime of the dynamo. It could therefore be connected with quenching, but in ways that are even qualitatively unclear. There are also aspects that might not be possible to capture within the framework of Cartesian geometry such as the extreme concentration of toroidal flux belts or wreaths (Brown et al. 2010), possibly connected with the dramatic concentration of kinetic helicity toward low latitudes and near the surface; see Figure 1(b) of Käpylä et al. (2012). One must therefore wait until proper test-field results for azimuthally averaged fields in spherical shells become available.

With these qualifications in mind, we have to content ourselves with statements that we can hope are robust. An example is our finding that the quenching exponents are of the order of unity and the prefactors typically below unity, which suggests that the quenched turbulent transport coefficients should not strongly deviate from their kinematic values if the magnetic field is comparable with the equipartition value. If our results should be employed in a mean-field dynamo model for the Sun, those obtained from convection simulations are the most relevant ones. Therefore, when restricting oneself to the coefficients α , η_t , and γ , one could think about choosing the quenching exponents 3, 2.3, and 2.3, respectively, in expressions of the form (32), with respect to $B_{\text{ext}}/B_{\text{eq0}}$, providing a somewhat stronger quenching than obtained with the

usually adopted exponent 2. However, given that dynamo fields are non-uniform, more elaborated models for the dependence of the transport coefficients on both the local \bar{B} and the local B_{eq0} , perhaps even also including a dependence on the local \bar{J} , need to be developed.

6. CONCLUSIONS

We have measured the quenching of the turbulent transport coefficients appearing in the mean-field dynamo equation, in particular α_{ij} , γ , η_{ij} , δ , and μ , by test-field methods. For this, we have considered three different background flows on which uniform external magnetic fields with various directions were imposed. This is of course quite different from the real situation where quenching occurs due to dynamo-generated mean fields; see Brandenburg et al. (2008b) for a measurement of α and η_t at large values of R_m in such a case. Another aspect to keep in mind is that the magnetic and fluid Reynolds numbers of our simulations are far too small in comparison with astrophysical situations. Extrapolation to $R_m \rightarrow \infty$ is feasible once an asymptotic regime is detected, but we emphasize that, in agreement with the results of Brandenburg et al. (2008b), our maximum value of $R_m \lesssim 600$ is not yet sufficient. Nevertheless, the obtained results indicate clear trends that may well apply to more realistic settings and parameter regimes.

In the setup with Roberts forcing, we have found as a striking property of the quenching behavior its dependence on whether one normalizes the external field with the actual or the original (unquenched) value of the equipartition field strength, B_{eq} or B_{eq0} , respectively. In the former case, the quenching exponent for turbulent diffusivity and α effect is significantly smaller and closer to that found for forced turbulence and convection (around 1.3). In the latter case, on the other hand, we recover the exponent 4, found earlier for α quenching in the Roberts flow (Rheinhardt & Brandenburg 2010). Somewhat surprisingly, we find the quenched α_{ij} and η_{ij} to be still isotropic in the xy plane, in contrast to that paper. However, it is now clear that this is a consequence of their use of a simplified momentum equation and that the obtained isotropy is physically sensible.

For isotropically forced turbulence, the differences between the two normalizations of B_{ext} are not so large and the exponent based on B_{eq0} is only around 1.5, which is higher than what has been found analytically in Kitchatinov et al. (1994) and Rogachevskii & Kleeorin (2000), while the exponent based on B_{eq} is around 1.1, which is similar to that found by Gressel et al. (2013).

Finally we have considered rotating stratified convection. Along with α and η_t , we have studied turbulent pumping (γ) and the $\boldsymbol{\Omega} \times \mathbf{J}$ effect (δ). We find that η_t and γ show similar quenching dependences on $B_{\text{ext}}/B_{\text{eq}}$ (with quenching exponent $q \approx 1.3$), while q is about 2 for α and δ . However, when B_{ext} is normalized with B_{eq0} the exponent becomes 3, which is in agreement with Rüdiger & Kitchatinov (1993). In non-rotating convection, the quenching of γ and η_t is only slightly weaker compared to the rotating case.

We have not studied the simultaneous quenching of turbulent transport by magnetic field and rotation, which is particularly important in rapidly rotating stars. Furthermore, we have not yet applied TFA for convection, which is a subject of our ongoing work. It is unclear, however, how useful it would be to consider quenching with this method, because only one preferred direction is possible. More general methods would be needed in the presence of a strong horizontal magnetic field.

We thank an anonymous referee for suggestions that improved the presentation. This work was supported in part by the European Research Council under the AstroDyn Research Project No. 227952, and the Swedish Research Council Grants No. 621-2011-5076 and 2012-5797, as well as the Research Council of Norway under the FRINATEK grant 231444. We acknowledge the allocation of computing resources provided by the Swedish National Allocations Committee at the Center for Parallel Computers at the Royal Institute of Technology in Stockholm and the National Supercomputer Centers in Linköping, the High Performance Computing Center North in Umeå, and the Nordic High Performance Computing Center in Reykjavik.

APPENDIX

QUENCHING FOR A SINGLE WAVE FLOW

Assume the forcing in Equation (8) to be a single transverse (frozen) wave with time-dependent amplitude,

$$f = \hat{f}(t) \hat{\mathbf{a}} \cos \psi, \quad \psi = \mathbf{k} \cdot \mathbf{x} + \phi, \\ \hat{\mathbf{a}} = \frac{\mathbf{k} \times \mathbf{e}}{|\mathbf{k} \times \mathbf{e}|}, \quad \mathbf{e} \nparallel \mathbf{k} - \text{an arbitrary vector.} \quad (\text{A1})$$

Then, in the absence of \mathbf{B}_{ext}

$$\mathbf{u}^{(0)} = \hat{\mathbf{a}} \cos \psi \int_{-\infty}^t \exp(\nu k^2(t' - t)) \hat{f}(t') dt' = \hat{u}^{(0)}(t) \hat{\mathbf{a}} \cos \psi, \\ p^{(0)} = \text{const}, \quad \rho^{(0)} = \text{const}, \quad (\text{A2})$$

is an exact solution of Equations (6) and (8) for arbitrary Re as, being a transverse wave, it obeys $\mathbf{u}^{(0)} \cdot \nabla \mathbf{u}^{(0)} = \mathbf{0}$, $\nabla \cdot \mathbf{u}^{(0)} = 0$ and $\nabla^2 \mathbf{u}^{(0)} = -k^2 \mathbf{u}^{(0)}$. Further,

$$\mathbf{b}^{(1)} = -B_{\text{ext}} k_x \hat{\mathbf{a}} \sin \psi \int_{-\infty}^t \exp(\eta k^2(t' - t)) \hat{u}^{(0)}(t') dt' \\ = -\hat{\beta}^{(1)}(t) B_{\text{ext}} k_x \hat{\mathbf{a}} \sin \psi \quad (\text{A3})$$

is an exact solution of the first-order induction equation with horizontal \mathbf{B}_{ext} for arbitrary R_m , again as a consequence of transversality and solenoidality of $\mathbf{u}^{(0)}$. Likewise,

$$\mathbf{u}^{(2)} \approx -B_{\text{ext}}^2 k_x^2 \hat{\mathbf{a}} \cos \psi \int_{-\infty}^t \exp(\nu k^2(t' - t)) \hat{\beta}^{(1)}(t') dt' / \rho^{(0)}, \\ p^{(2)} \approx -\mathbf{b}^{(1)2} / 2 - \mathbf{b}^{(1)} \cdot \mathbf{B}_{\text{ext}}, \quad (\text{A4})$$

is an approximate solution of the second-order momentum equation as long as $p^{(2)} \ll p^{(0)}$, thus $\rho \approx \rho^{(0)}$. As $\mathbf{u}^{(2)} \sim \mathbf{u}^{(0)}$ (with a time-dependent factor) the argument continues to hold in arbitrary orders in B_{ext} . The relation $\mathbf{u}^{(2)} \sim \mathbf{u}^{(0)}$ would even hold for the less restricting condition that only the non-constant part of $p^{(2)}$ needs to be negligible. We conclude that the imposed field does not change the geometry of the flow, but only its amplitude. Considering an ensemble of such flows with randomly chosen \mathbf{k} and \mathbf{e} , the transport coefficients obtained by ensemble averaging would have to be isotropic, even when quenched, as long as the density remains close to uniform.

REFERENCES

- Blackman, E. G., & Brandenburg, A. 2002, *ApJ*, **579**, 359
- Braginsky, S. I. 1964, *Ge&Ae*, **4**, 572
- Brandenburg, A. 2001, *ApJ*, **550**, 824
- Brandenburg, A., Gressel, O., Käpylä, P. J., et al. 2013, *ApJ*, **762**, 127
- Brandenburg, A., Jennings, R. L., Nordlund, Å., et al. 1996, *JFM*, **306**, 325
- Brandenburg, A., Moss, D., & Tuominen, I. 1992, in ASP Conf. Ser. 27, The Solar Cycle, ed. K. L. Harvey (San Francisco, CA: ASP), 536
- Brandenburg, A., Nordlund, Å., Pulkkinen, P., Stein, R. F., & Tuominen, I. 1990, *A&A*, **232**, 277
- Brandenburg, A., Rädler, K.-H., & Kemel, K. 2012, *A&A*, **539**, A35
- Brandenburg, A., Rädler, K.-H., Rheinhardt, M., & Käpylä, P. J. 2008a, *ApJ*, **676**, 740
- Brandenburg, A., Rädler, K.-H., Rheinhardt, M., & Subramanian, K. 2008b, *ApJL*, **687**, L49
- Brandenburg, A., Rädler, K.-H., & Schinner, M. 2008c, *A&A*, **482**, 739
- Brown, B. P., Browning, M. K., Brun, A. S., Miesch, M. S., & Toomre, J. 2010, *ApJ*, **711**, 424
- Brun, A. S., Miesch, M. S., & Toomre, J. 2004, *ApJ*, **614**, 1073
- Bykov, A. M., Brandenburg, A., Malkov, M. A., & Osipov, S. M. 2013, *SSRv*, **178**, 201
- Cattaneo, F., & Hughes, D. W. 1996, *PhRvE*, **54**, R4532
- Cattaneo, F., & Vainshtein, S. I. 1991, *ApJL*, **376**, L21
- Charbonneau, P. 2010, *LRSF*, **7**, 3
- Chatterjee, P., Nandy, D., & Choudhuri, A. R. 2004, *A&A*, **427**, 1019
- Choudhuri, A. R., & Gilman, P. A. 1987, *ApJ*, **316**, 788
- Choudhuri, A. R., & Karak, B. B. 2009, *RAA*, **9**, 953
- Choudhuri, A. R., & Karak, B. B. 2012, *PhRvL*, **109**, 171103
- Covas, E., Tavakol, R., Tworkowski, A., & Brandenburg, A. 1998, *A&A*, **329**, 350
- Del Sordo, F., Guerrero, G., & Brandenburg, A. 2013, *MNRAS*, **429**, 1686
- Do Cao, O., & Brun, A. S. 2012, *AN*, **332**, 907
- D'Silva, S., & Choudhuri, A. R. 1993, *A&A*, **272**, 621
- Gilman, P. A. 1983, *ApJS*, **53**, 243
- Gilman, P. A., & Miller, J. 1981, *ApJ*, **46**, 211
- Glatzmaier, G. A. 1985, *ApJ*, **291**, 300
- Gressel, O., Bendre, A., & Elstner, D. 2013, *MNRAS*, **429**, 967
- Guerrero, G., & de Gouveia Dal Pino, E. M. 2008, *ApJ*, **485**, 267
- Guerrero, G., Dikpati, M., & de Gouveia Dal Pino, E. M. 2009, *ApJ*, **701**, 725
- Heinemann, T., McWilliams, J. C., & Schekochihin, A. A. 2011, *PhRvL*, **107**, 255004
- Hubbard, A., & Brandenburg, A. 2009, *ApJ*, **706**, 712
- Hubbard, A., Del Sordo, F., Käpylä, P. J., & Brandenburg, A. 2009, *MNRAS*, **398**, 1891
- Hurlburt, N. E., Toomre, J., & Massaguer, J. M. 1986, *ApJ*, **311**, 563
- Jepps, S. A. 1975, *JFM*, **67**, 625
- Jiang, J., Chatterjee, P., & Choudhuri, A. R. 2007, *MNRAS*, **381**, 1527
- Käpylä, P. J., & Brandenburg, A. 2009, *ApJ*, **699**, 1059
- Käpylä, P. J., Korpi, M. J., & Brandenburg, A. 2008, *A&A*, **491**, 353
- Käpylä, P. J., Korpi, M. J., & Brandenburg, A. 2009a, *A&A*, **500**, 633
- Käpylä, P. J., Korpi, M. J., & Brandenburg, A. 2009b, *ApJ*, **697**, 1153
- Käpylä, P. J., Korpi, M. J., & Tuominen, I. 2006, *AN*, **327**, 884
- Käpylä, P. J., Mantere, M. J., & Brandenburg, A. 2012, *ApJ*, **755**, 22
- Käpylä, P. J., Mantere, M. J., Cole, E., Warnecke, J., & Brandenburg, A. 2013, *ApJ*, **778**, 41
- Karak, B. B. 2010, *ApJ*, **724**, 1021
- Karak, B. B., & Choudhuri, A. R. 2011, *MNRAS*, **410**, 1503
- Karak, B. B., & Choudhuri, A. R. 2012, *SoPh*, **278**, 137
- Karak, B. B., & Choudhuri, A. R. 2013, *RAA*, **13**, 1339
- Karak, B. B., & Käpylä, P. J., Käpylä, M. J., & Brandenburg, A. 2014, *A&A*, in press (arXiv:1407.0984)
- Karak, B. B., & Nandy, D. 2012, *ApJL*, **761**, L13
- Kitchatinov, L. L., & Pipin, V. V. 1993, *A&A*, **274**, 647
- Kitchatinov, L. L., Pipin, V. V., & Rüdiger, G. 1994, *AN*, **315**, 157
- Kleeorin, N., Moss, D., Rogachevskii, I., & Sokoloff, D. 2000, *A&A*, **361**, L5
- Kleeorin, N. I., & Ruzmaikin, A. A. 1982, *MHD*, **18**, 116
- Köhler, H. 1973, *A&A*, **25**, 467
- Krause, F., & Rädler, K.-H. 1980, Mean-Field Magnetohydrodynamics and Dynamo Theory (Berlin: Akademie; Oxford: Pergamon)
- Mitra, D., & Brandenburg, A. 2012, *MNRAS*, **420**, 2170
- Mitra, D., Käpylä, P. J., Tavakol, R., & Brandenburg, A. 2009, *A&A*, **495**, 1
- Moffatt, H. K. 1972, *JFM*, **53**, 385
- Muñoz-Jaramillo, A., Nandy, D., & Martens, P. C. H. 2011, *ApJL*, **727**, L23
- Ossendrijver, M., Stix, M., & Brandenburg, A. 2001, *A&A*, **376**, 713
- Parker, E. N. 1955, *ApJ*, **122**, 293
- Pipin, V. V., & Kosovichev, A. G. 2011, *ApJL*, **727**, L45
- Pipin, V. V., & Kosovichev, A. G. 2014, *ApJ*, **785**, 49
- Pipin, V. V., & Seehafer, N. 2009, *A&A*, **493**, 819
- Pouquet, A., Frisch, U., & Léorat, J. 1976, *JFM*, **77**, 321
- Racine, E., Charbonneau, P., Ghizaru, M., Bouchat, A., & Smolarkiewicz, P. K. 2011, *ApJ*, **735**, 46
- Rädler, K.-H. 2014, *AN*, **335**, 459
- Rädler, K.-H., Rheinhardt, M., Apstein, E., & Fuchs, H. 2002, *MHD*, **38**, 39
- Rempel, M. 2006, *ApJ*, **647**, 662
- Rheinhardt, M., & Brandenburg, A. 2010, *A&A*, **520**, 28
- Rheinhardt, M., & Brandenburg, A. 2012, *AN*, **333**, 71
- Rheinhardt, M., Devlen, E., Rädler, K.-H., & Brandenburg, A. 2014, *MNRAS*, **441**, 116
- Roberts, G. O. 1972, *RSPTA*, **271**, 411
- Roberts, P. H., & Soward, A. M. 1975, *AN*, **296**, 49
- Rogachevskii, I., & Kleeorin, N. 2000, *PhRvE*, **61**, 5202
- Rogachevskii, I., & Kleeorin, N. 2001, *PhRvE*, **64**, 056307
- Rogachevskii, I., & Kleeorin, N. 2003, *PhRvE*, **68**, 036301
- Rogachevskii, I., & Kleeorin, N. 2006, *GApFD*, **100**, 243
- Rogachevskii, I., Kleeorin, N., Brandenburg, A., & Eichler, D. 2012, *ApJ*, **753**, 6
- Rüdiger, G. 1974, *AN*, **295**, 275
- Rüdiger, G., & Brandenburg, A. 1995, *A&A*, **296**, 557
- Rüdiger, G., & Kitchatinov, L. L. 1993, *AN*, **269**, 581
- Rüdiger, G., & Kitchatinov, L. L. 2000, *AN*, **321**, 75
- Rüdiger, G., Kitchatinov, L. L., Küker, M., & Schultz, M. 1994, *GApFD*, **78**, 247
- Schrinner, M., Rädler, K.-H., Schmitt, D., Rheinhardt, M., & Christensen, U. 2005, *AN*, **326**, 245
- Schrinner, M., Rädler, K.-H., Schmitt, D., Rheinhardt, M., & Christensen, U. R. 2007, *GApFD*, **101**, 81
- Steenbeck, M., Krause, F., & Rädler, K.-H. 1966, *ZNatA*, **21**, 369
- Stix, M. 2002, The Sun: An Introduction (Berlin: Springer)
- Sur, S., Brandenburg, A., & Subramanian, K. 2008, *MNRAS*, **385**, L15
- Sur, S., Subramanian, K., & Brandenburg, A. 2007, *MNRAS*, **376**, 1238
- Vainshtein, S. I., & Cattaneo, F. 1992, *ApJ*, **393**, 165
- Vishniac, E. T., & Brandenburg, A. 1997, *ApJ*, **475**, 263
- Weber, M., Fan, Y., & Miesch, M. S. 2011, *ApJ*, **741**, 11
- Yeates, A. R., Nandy, D., & Mackay, D. H. 2008, *ApJ*, **673**, 544
- Yousef, T. A., Brandenburg, A., & Rüdiger, G. 2003, *A&A*, **411**, 321

Queries

Page 16

Q1

Author: Please check the details for any journal references that do not have a pale purple link (CrossRef doi) or a blue link (NASA ADS or arXiv e-print) in the two-column proof (article-style layout). A journal reference with no links may contain some incorrect information.

Online-only colour figures

This proof PDF is identical in specification to the PDF file that will be published in the online journal. To view any online-only color figures as they will appear in the printed journal, we recommend that this color PDF file be printed on a black & white printer.